

博士論文（要約）

Charge neutral current generation
and phase transitions
in quantum Hall antiferromagnet
of bilayer graphene

(2 層グラフェンの量子ホール反強磁性状態
における非電荷流生成と相転移)

田中 未羽子

Contents

1	Introduction	2
1.1	Electron internal degrees of freedom	2
1.1.1	Ordering and phase transition	2
1.1.2	Charge neutral currents	2
1.2	Motivation and outline of the thesis	3
2	Basic electronic property of graphene	5
2.1	Band structure	5
2.1.1	Tight-binding model	5
2.1.2	Low energy effective Hamiltonian of monolayer graphene	7
2.1.3	Low energy effective Hamiltonian of bilayer graphene	9
2.1.4	Low energy effective Hamiltonian of ABA-stacked trilayer graphene	12
2.2	Quantum Hall effect of graphene	15
2.2.1	Two-dimensional free electron gas	15
2.2.2	Monolayer graphene	16
2.2.3	Bilayer graphene	18
3	Charge neutral currents in graphene	20
3.1	Spintronics in graphene	20
3.1.1	Spin current injection and transport	20
3.1.2	Spin Hall effect	23
3.2	Valleytronics in graphene	25
3.2.1	Berry curvature	25
3.2.2	Valley Hall effect	28
4	Quantum Hall ferromagnetism	34
4.1	Electron correlation energy v.s. Kinetic energy	34
4.2	Quantum Hall ferromagnetism	35
4.3	Generalized quantum Hall ferromagnetism with multiple internal degrees of freedom of an electron	37
4.3.1	Quantum Hall ferromagnetism with layers DOF	37
4.3.2	Quantum Hall ferromagnetism with spins and layers DOFs	40
4.4	$\nu = 0$ state of graphene	41
5	Charge neutral current generation in quantum Hall antiferromagnet of bi-layer graphene	47
5.1	Motivation	47
5.2	Proposal of spin-valley Hall effect	48
5.3	Nonlocal transport measurement	49
5.4	Sample fabrication	51

5.5	Dual gate dependence	53
5.6	Scaling relationship	56
5.7	Elimination of other possible origins of nonlocal resistance	60
5.7.1	Current leakage through voltage measurement terminals	60
5.7.2	Ohmic current diffusion	62
5.7.3	Capacitance effect	62
5.7.4	Thermal effect	62
5.7.5	Edge transport	64
5.8	Conclusion and perspectives	65
6	Phase transition in quantum Hall antiferromagnet of bilayer graphene	67
6.1	Motivation	67
6.2	Sample structure	68
6.3	Experimental result	68
6.4	Discussions	68
7	Weak localization in ABA-stacked trilayer graphene	69
7.1	Motivation	69
7.2	Sample fabrication	69
7.3	Experimental result	69
7.4	Discussions	69
8	Summary and Outlook	70

Chapter 1

Introduction

1.1 Electron internal degrees of freedom

1.1.1 Ordering and phase transition

Existence of internal degrees of freedom (DOFs) of electrons such as the spin, sublattice, layer, valley, multiple bands, etc. is the origin of variety of physical phenomena in condensed matters.

One of the most important phenomena is ordering of internal DOFs by the electron-electron interaction. The spin DOF gives rise to varieties of magnetism such as ferromagnetism, antiferromagnetism, ferrimagnetism, and frustrated magnetism. Sublattice or layer DOF also leads to ordered states such as the ferroelectric state, layer coherent state, etc.

Phase transitions are inseparable phenomena from the ordering of internal DOFs. Usually, increase of the temperature results in an ordered-to-disordered phase transition. Phase transitions are also induced at zero temperature by the change of parameters such as the carrier density, electric field, magnetic field, pressure, etc., which are called quantum phase transition.

In particular, strongly correlated electron systems exhibit drastic change of the states by a small change of the parameter, and therefore serve as playgrounds for fertile phase transitions. The examples of such strongly correlated systems are the cuprates and molecular crystals, which exhibit Mott transitions, Moire heterostructures of two-dimensional van der Waals materials, and quantum Hall systems (Fig. 1.1). A common feature of them is the large density of states, which suppresses the kinetic energy and relatively enhances the interaction energy (detail is discussed in Chapter 4). Correlated electron systems are not only interesting, but also promising for application owing to their high tunability.

1.1.2 Charge neutral currents

In addition to the ordering and phase transitions, another important phenomenon related to the internal DOFs is the flow of them without net charge current, which is called charge neutral current. The most typical example is the spin current, which is the flow of spin DOF. The valley current is another example, where electrons belonging to different valleys in the band structure flow into different directions. The valley DOF is a well-defined quantum two-level system in hexagonal lattices such as graphene and transition metal dichalcogenides (TMD). Charge neutral currents are generally less-dissipative than the charge current, therefore promising for future low power consumption devices.

Researches on charge neutral current have been done for metals, semiconductors, and magnetic insulators (Fig. 1.1). In metals, semiconductors, and graphene, the pure spin (or valley) current is the flow of electrons into opposite directions between those with different spin (or valley), where the net charge current is zero. In magnetic insulators, electrons do not move, but collective motion of spins carries a flow of spin, which is called spin wave. In either case, previous researches on charge neutral currents are done for systems or states, where the electronic correlation does not play an important role (Fig. 1.1).

One of the techniques to generate a charge neutral current is flavor Hall effect, such as the spin Hall effect and the valley Hall effect. Here, electrons with different flavors (internal DOFs) have opposite sign of the Hall conductivity, therefore a charge neutral current is generated perpendicularly to the injected charge current. Previously-known origins of flavor dependent Hall conductivity is the spin orbit interaction for spin, and the Berry curvature induced by spatial inversion symmetry breaking for valley (detail is discussed in Chapter 3). Both mechanisms are described in a one-particle picture.

1.2 Motivation and outline of the thesis

Based on the background discussed above, we aim to investigate an unexplored field, charge neutral current generation in a highly correlated electron system (the orange broken rectangle in Fig. 1.1). To utilize the high tunability of electron correlation, the mechanism to produce a flavor dependent Hall conductivity should originate from the electron correlation. We employ quantum Hall state of bilayer graphene since it is gate-tunable and relatively robust against temperature. At half filling of the Landau level at zero energy, electron correlation leads to antiferromagnetic ordering in association with a spontaneous breaking of the spatial inversion symmetry, which results in a flavor dependent Hall conductivity.

We propose the charge neutral current generation using this flavor dependent Hall conductivity and demonstrate it by the nonlocal transport measurement (Chapter 5). In addition to that the flavor Hall effect originates from a new mechanism due to electron correlation, the Hall conductivity in this state is spin and valley contrasting. Therefore, generated charge neutral current is not a spin current nor a valley current, but opposite valley currents for opposite spins. Such a combined charge neutral current of spin and valley will provide a new method to couple spin and valley DOFs in graphene.

Since quantum Hall magnetic states in graphene are more robust than those in semiconductor-based conventional two-dimensional systems owing to stronger electronic correlation, they are good platforms for experimental study of various phase transitions. In Chapter 6, we aim to reveal phase diagram of quantum phase transitions and a temperature-induced phase transition in quantum Hall antiferromagnetic state of bilayer graphene. We fabricate Corbino devices to measure bulk conductivity and its temperature dependence. Combined with the temperature dependence of the nonlocal transport (charge neutral current generation), we propose that the temperature-induced phase transition consists of two steps.

Chapter 7 presents a little different topic from Chapter 5 and 6. We investigated ABA-stacked trilayer graphene, which has an electron internal DOF originated from coexistence of two bands. One band has linear dispersion and Berry phase of π similarly to monolayer graphene, while the other band has parabolic dispersion and Berry phase of 2π similarly to bilayer graphene. Effects of the coexistence of these bands on transport property has not been explored so much. Here, we study this problem by measuring a weak localization effect in magnetoconductance.

Chapters 2~4 present background knowledges necessary to understand Chapters 5~7. In Chapter 2, basic electronic properties of monolayer, bilayer, and trilayer graphene are discussed. In Chapter 3, previous experimental studies on charge neutral currents in graphene are introduced. In Chapter 4, theory of electron correlation in the quantum Hall state are provided.

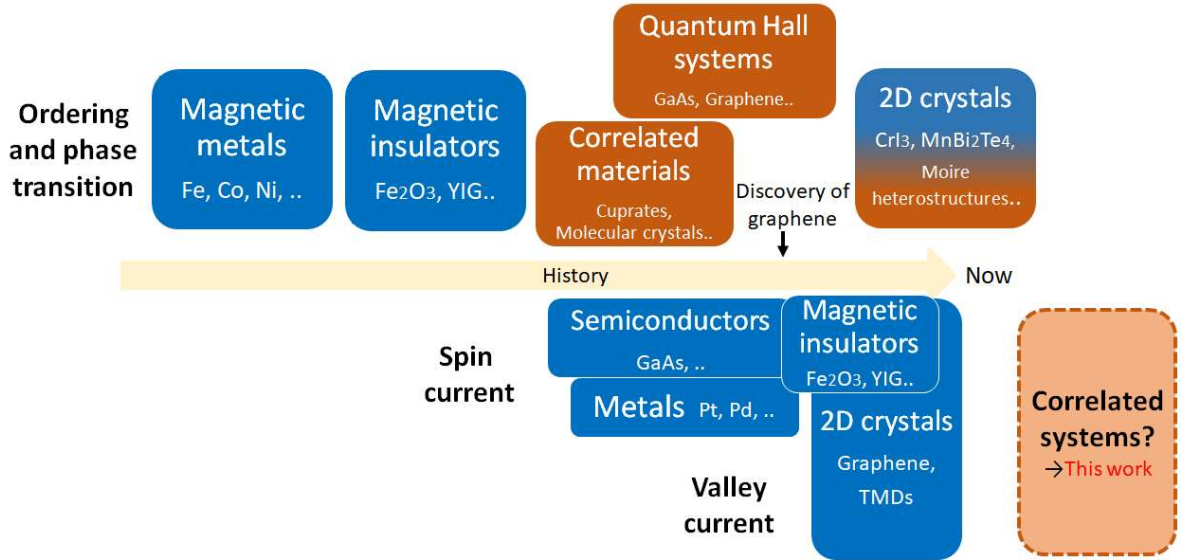


Figure 1.1: Schematic of the playgrounds of the electron internal degrees of freedom. Upper material classes are used for the study of magnetism and phase transitions, and lower material classes are used for the study of charge neutral currents. Blue and orange colors denote uncorrelated systems and correlated systems, respectively.

Chapter 2

Basic electronic property of graphene

2.1 Band structure

In this section, we first derive the band structure of monolayer graphene using tight-binding model (1.1.1) and obtain the low energy effective Hamiltonian (1.1.2). Using the result, we derive the low energy effective Hamiltonian of bilayer graphene (1.1.3).

2.1.1 Tight-binding model

Monolayer graphene is a two-dimensional honeycomb lattice of carbon atoms. A honeycomb lattice is not a Bravais lattice but a triangle lattice is a Bravais lattice, so we consider the set of two carbon atoms as a unit cell (Fig. 2.1). Two carbon sites in a unit cell are called A and B site.

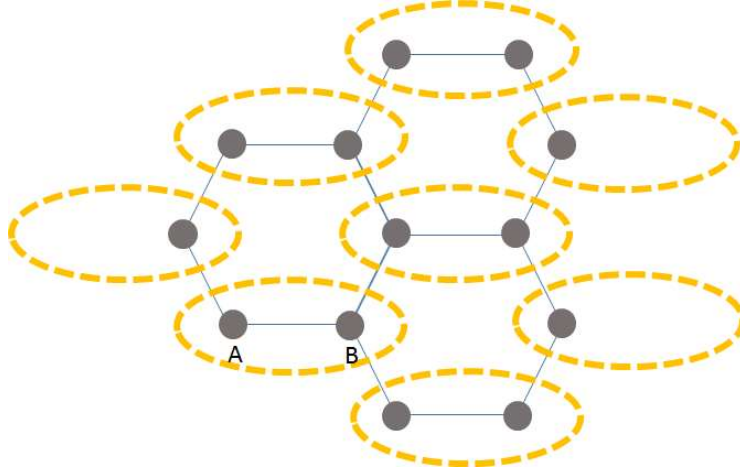


Figure 2.1: Lattice structure of monolayer graphene. Gray points indicate carbon atoms and orange circles indicate unit cells.

With the creation operators a^\dagger and b^\dagger for each sites, tight-binding Hamiltonian with nearest neighbor hopping is written as,

$$H = -t \sum_{i=1}^N \sum_{j=1}^3 a^\dagger(\mathbf{R}_i) b(\mathbf{R}_i + \delta_j) + h.c. . \quad (2.1)$$

Here, t is the nearest neighbor hopping energy, \mathbf{R}_i is the position of A site in the i -th unit cell, and δ_j is the differential vector from a A site to its neighboring three B sites. Using the creation and annihilation operators in k -space defined by

$$a^\dagger(\mathbf{R}_i) = \frac{1}{\sqrt{N}} \sum_{\mathbf{k}} a_{\mathbf{k}}^\dagger \exp(-i\mathbf{k} \cdot \mathbf{R}_i) \quad (2.2)$$

$$b(\mathbf{R}_i + \delta_j) = \frac{1}{\sqrt{N}} \sum_{\mathbf{k}} b_{\mathbf{k}} \exp(-i\mathbf{k} \cdot (\mathbf{R}_i + \delta_j)), \quad (2.3)$$

we can rewrite Eq.2.1 as following:

$$H = -t \sum_{\mathbf{k}} \sum_{j=1}^3 \exp(i\mathbf{k} \cdot \delta_j) a_{\mathbf{k}}^\dagger b_{\mathbf{k}} + h.c.. \quad (2.4)$$

Eq. 2.4 is expressed in matrix representation:

$$H = \sum_{\mathbf{k}} \begin{pmatrix} a_{\mathbf{k}}^\dagger & b_{\mathbf{k}}^\dagger \end{pmatrix} \begin{pmatrix} 0 & D(\mathbf{k}) \\ D^*(\mathbf{k}) & 0 \end{pmatrix} \begin{pmatrix} a_{\mathbf{k}} \\ b_{\mathbf{k}} \end{pmatrix}. \quad (2.5)$$

Here, $D(\mathbf{k}) \equiv -t \sum_{j=1}^3 \exp(i\mathbf{k} \cdot \delta_j)$.

By diagonalizing the 2×2 matrix

$$H_{\mathbf{k}} = \begin{pmatrix} 0 & D(\mathbf{k}) \\ D^*(\mathbf{k}) & 0 \end{pmatrix}, \quad (2.6)$$

we obtain the eigenenergy

$$\begin{aligned} E_{\mathbf{k}} &= \pm |D(\mathbf{k})| \\ &= \pm \sqrt{3 + 2 \cos(\sqrt{3}k_x a) + 4 \cos(\frac{\sqrt{3}}{2}k_x a) \cos(\frac{3}{2}k_y a)}. \end{aligned} \quad (2.7)$$

This is shown as a band structure in Fig. 2.2.

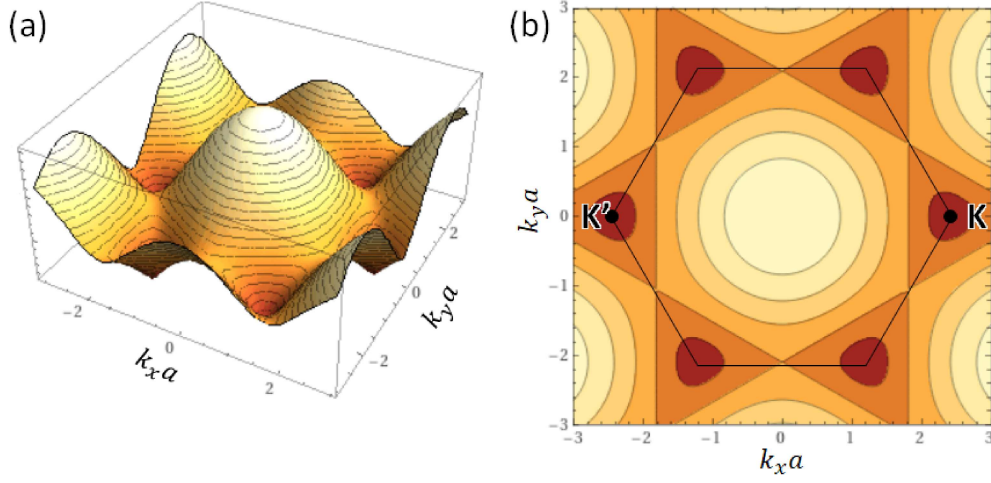


Figure 2.2: Schematic tight-binding band structure of monolayer graphene. (a) Conduction band of monolayer graphene obtained from Eq. 2.7. (b) Contours of (a). Black hexagon indicates the first Brillouin zone. K point and K' point are indicated by black dots.

We can see zero energy band touching points at the corner of Brillouin zone, which are called Dirac points. Six corners of Brillouin zone are classified into two nonequivalent groups originated from the nonequivalency of A site and B site, which are called K point and K' point.

An electron near the Fermi surface has an options of existing at K point (K valley) or K' point (K' valley), which is called valley degree of freedom (DOF).

2.1.2 Low energy effective Hamiltonian of monolayer graphene

By expanding Eq. 2.6 near the Dirac point, we derive the low energy effective Hamiltonian. Near the K and K' point, $D(k)$ is expanded as

$$\begin{aligned}
 D(\mathbf{K} + \mathbf{k}) &= -t \sum_{j=1}^3 \exp(i(\mathbf{K} + \mathbf{k}) \cdot \boldsymbol{\delta}_j) \\
 &\simeq -t \sum_{j=1}^3 (1 + i\mathbf{k} \cdot \boldsymbol{\delta}_j) \exp(i\mathbf{K} \cdot \boldsymbol{\delta}_j) \\
 &= \frac{3}{2} ta (k_x - ik_y)
 \end{aligned} \tag{2.8}$$

and

$$D(\mathbf{K}' + \mathbf{k}) = \frac{3}{2} ta (-k_x - ik_y), \tag{2.9}$$

respectively.

Therefore, the low energy Hamiltonian is expressed by

$$\begin{aligned} H_\tau(\mathbf{k}) &= \frac{3}{2}ta \begin{pmatrix} 0 & \tau k_x - ik_y \\ \tau k_x + ik_y & 0 \end{pmatrix} \\ &= \hbar v_F (\tau k_x \sigma_x + k_y \sigma_y). \end{aligned} \quad (2.10)$$

Here, τ is the indicator of valley DOF which takes the value of 1(-1) for K(K') valley, $v_F = 3ta/2\hbar$ is the Fermi velocity, and σ_x and σ_y are Pauli matrix of sublattices.

This Hamiltonian is similar to Dirac Hamiltonian. While the basis of Pauli matrix is spin in Dirac equation, the basis of this effective Hamiltonian is the presence of an electron in A site and B site. Based on this analogy, the DOF of sublattice A and B is called pseudospin.

In general, Hamiltonian $H = \mathbf{R} \cdot \boldsymbol{\sigma}$ in a form of inner product between Pauli matrix and any vector $\mathbf{R} = R(\sin \theta \cos \phi, \sin \theta \sin \phi, \cos \theta)$ has the eigenenergy and eigenstates of

$$E = \pm |R|, \quad \psi = \begin{pmatrix} \cos \frac{\theta}{2} \\ \pm e^{i\phi} \sin \frac{\theta}{2} \end{pmatrix}. \quad (2.11)$$

Using this knowledge, we can derive the eigenenergy and eigenstates of Eq. 2.10 as following,

$$E(\mathbf{k}) = \pm \hbar v_F k, \quad \psi(\mathbf{k}) = \frac{1}{\sqrt{2}} \begin{pmatrix} 1 \\ \pm e^{i\phi} \end{pmatrix} \quad \text{for K valley}, \quad (2.12)$$

$$E(\mathbf{k}) = \pm \hbar v_F k, \quad \psi(\mathbf{k}) = \frac{1}{\sqrt{2}} \begin{pmatrix} 1 \\ \pm e^{-i\phi} \end{pmatrix}, \quad \text{for K' valley}. \quad (2.13)$$

while $k \cos \phi = k_x$ and $k \sin \phi = k_y$.

Fig. 2.3 shows the schematic of band structure based on Eq. 2.12 and 2.13. Red arrows indicate the direction of sublattice pseudospin eigenstates $\psi(\mathbf{k})$. We can see that the pseudospin makes one rotation in association with one loop around a Dirac point in k -space. The direction of rotation is inversed for K valley and K' valley. This is the origin of valley dependent Berry curvature, which will be explained in Chapter 3.

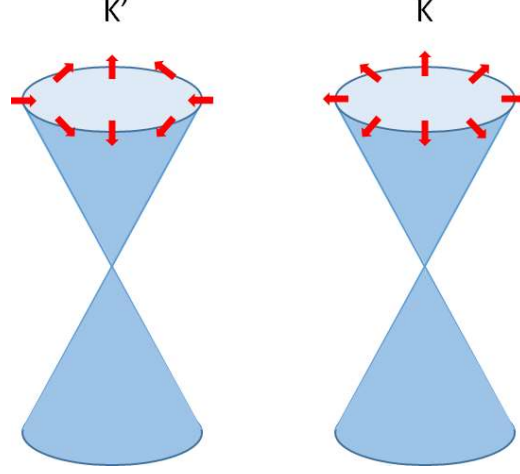


Figure 2.3: Schematic of pseudospin orientation in low energy band structure of monolayer graphene.

When potential difference 2Δ is introduced between A site and B site, low energy Hamiltonian is modified to

$$\begin{aligned}
 H_{\tau}(\mathbf{k}) &= \frac{3}{2}ta \begin{pmatrix} \Delta & \tau k_x - ik_y \\ \tau k_x + ik_y & -\Delta \end{pmatrix} \\
 &= \hbar v_F(\tau k_x \sigma_x + k_y \sigma_y) + \Delta \sigma_z.
 \end{aligned} \tag{2.14}$$

This can be interpreted as the application of z-axis magnetic field for pseudospin, so we can expect mixing of in-plane pseudospin, which leads to anticrossing of the band at the Dirac points.

By diagonalizing Eq. 2.14, we obtain the band structure with energy gap $E(\mathbf{k}) = \pm \sqrt{(\hbar v_F k)^2 + \Delta^2}$ opening at Dirac points.

2.1.3 Low energy effective Hamiltonian of bilayer graphene

Bilayer graphene is composed of two layers of monolayer graphene with a parallel displacement by the length of lattice constant (Fig. 2.4). It has four atoms, A1, B1, A2, and B2 in one unit cell.

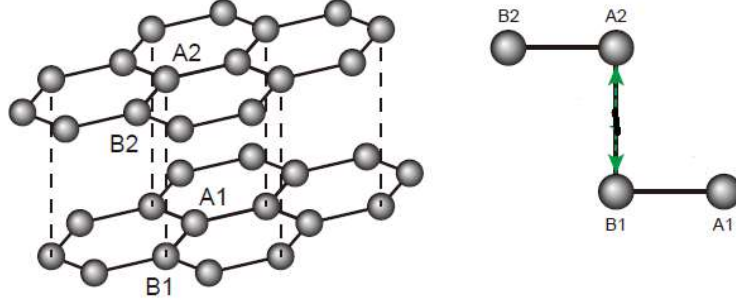


Figure 2.4: Crystal structure of bilayer graphene.

Since the interlayer hopping energy between A2 and B1 is stronger than other interlayer hopping energy, we only take A2-B1 hopping into account as the interlayer hopping (green arrow in Fig. 2.4). Based on this assumption, Hamiltonian is written with the basis of A1, B1, A2, B2 sites:

$$H = \begin{pmatrix} & & 0 & 0 \\ & H_{1L} & -\gamma & 0 \\ 0 & -\gamma & & \\ 0 & 0 & H_{1L} & \end{pmatrix}, \quad (2.15)$$

where H_{1L} is the Hamiltonian of monolayer graphene defined in Eq. 2.10.

Performing unitary transformation

$$U = \begin{pmatrix} 1 & 0 & 0 & 0 \\ 0 & 0 & 0 & 1 \\ 0 & 0 & 1 & 0 \\ 0 & 1 & 0 & 0 \end{pmatrix}, \quad (2.16)$$

we can transform Eq. 2.15 into

$$\begin{aligned} \tilde{H} &= U^{-1} H U \\ &= \begin{pmatrix} & 0 & H_{1L} & \\ - & - & 0 & -\gamma \\ H_{1L} & -\gamma & & 0 \end{pmatrix} \\ &= \begin{pmatrix} 0 & H_{1L} \\ H_{1L} & -\Gamma \end{pmatrix}, \end{aligned} \quad (2.17)$$

with

$$\Gamma = \begin{pmatrix} 0 & \gamma \\ \gamma & 0 \end{pmatrix} \quad (2.18)$$

and the new basis is (A1, B2, A2, B1).

When we define the eigenstates of \tilde{H} with

$$\begin{pmatrix} u^L \\ u^H \end{pmatrix}, \quad (2.19)$$

following relationship hold for them

$$\begin{pmatrix} 0 & H_{1L} \\ H_{1L} & -\Gamma \end{pmatrix} \begin{pmatrix} u^L \\ u^H \end{pmatrix} = E \begin{pmatrix} u^L \\ u^H \end{pmatrix} \quad (2.20)$$

$$\begin{aligned} \rightarrow \quad H_{1L}u^H &= Eu^L \\ H_{1L}u^L - \Gamma u^H &= Eu^H. \end{aligned} \quad (2.21)$$

By substituting Eq. (1.23) to Eq(1.22),

$$\begin{aligned} H_{1L}u^L &= (E + \Gamma)EH_{1L}^{-1}u^L \\ H_{1L}(E + \Gamma)^{-1}H_{1L}u^L &= Eu^L \end{aligned} \quad (2.22)$$

holds.

Since we consider the low energy regime $E \ll \gamma$,

$$\begin{aligned} H_{1L}(E + \Gamma)^{-1}H_{1L}u^L &= H_{1L} \begin{pmatrix} E & \gamma \\ \gamma & E \end{pmatrix}^{-1} H_{1L} \\ &= H_{1L} \frac{1}{E^2 - \gamma^2} \begin{pmatrix} E & -\gamma \\ -\gamma & E \end{pmatrix} H_{1L} \\ &\simeq \frac{1}{\gamma} H_{1L} \sigma_x H_{1L} \\ &= \frac{(\hbar v_F)^2}{\gamma} (\tau k_x \sigma_x + k_y \sigma_y) \sigma_x (\tau k_x \sigma_x + k_y \sigma_y) \\ &= \frac{(\hbar v_F)^2}{\gamma} [(k_x^2 - k_y^2) \sigma_x + 2\tau k_x k_y \sigma_y] \\ &= \frac{(\hbar v_F)^2 k^2}{\gamma} [\cos 2\phi \sigma_x + \tau \sin 2\phi \sigma_y] \\ &= \frac{(\hbar v_F)^2}{\gamma} \begin{pmatrix} 0 & (\tau k_x - i k_y)^2 \\ (\tau k_x + i k_y)^2 & 0 \end{pmatrix}, \end{aligned} \quad (2.23)$$

with $k \cos \phi = k_x$ and $k \sin \phi = k_y$.

When E is small, $|u^H|$ become small according to Eq. (1.22). This means that low energy states have larger amplitude on A1 and B2 sites. Therefore we shrink the four-component basis to two-component basis of A1 and B2, then obtain the low energy 2×2 effective Hamiltonian,

$$H_{2L} = \frac{(\hbar v_F)^2 k^2}{\gamma} [\cos 2\phi \sigma_x + \tau \sin 2\phi \sigma_y]. \quad (2.24)$$

The eigenenergy and eigenstate are

$$E(\mathbf{k}) = \pm \frac{(\hbar v_F)^2 k^2}{\gamma}, \quad \psi(\mathbf{k}) = \begin{pmatrix} 1 \\ \pm e^{2i\phi} \end{pmatrix} \quad (2.25)$$

for K valley, and

$$E(\mathbf{k}) = \pm \frac{(\hbar v_F)^2 k^2}{\gamma}, \quad \psi(\mathbf{k}) = \begin{pmatrix} 1 \\ \pm e^{-2i\phi} \end{pmatrix} \quad (2.26)$$

for K' valley.

The band structure has parabolic dispersion and its effective mass is $m^* = \frac{\gamma}{2v_F^2}$. Pseudospin makes two rotations in association with one loop around the Dirac points in k-space (Fig. 2.5).

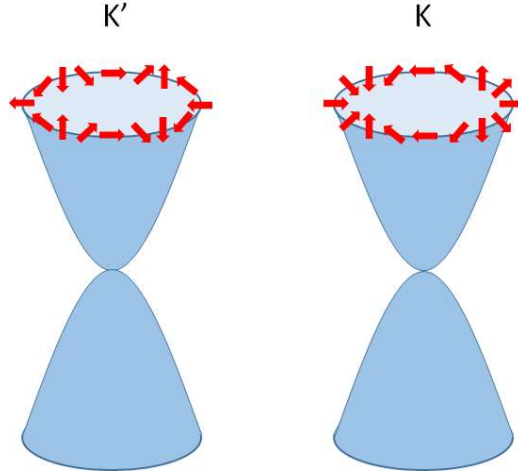


Figure 2.5: Schematic of pseudospin in the band structure of bilayer graphene.

When potential difference of 2Δ between the layers is introduced, energy gap opens at zero energy similarly to monolayer graphene $E(\mathbf{k}) = \pm \sqrt{\left[\frac{(\hbar v_F)^2 k^2}{\gamma}\right]^2 + \Delta^2}$. This is realized by applying an out-of-plane electric field.

2.1.4 Low energy effective Hamiltonian of ABA-stacked trilayer graphene

Trilayer graphene has two types of stacking, ABA-stacking and ABC-stacking. In both stacking, the first and second two layers are the same with bilayer graphene. The third layer is

exactly on top of the first layer in ABA-stacking, while it is shifted from the second layer in the same way as the first and second layers are shifted in ABC-stacking. ABA-stacking is the most stable state and ABC-stacking is a metastable state.

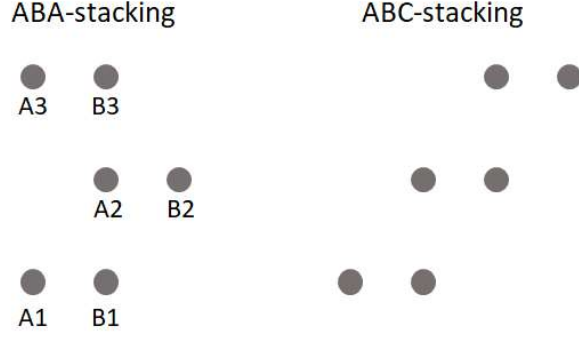


Figure 2.6: Schematic of ABA-stacking and ABC-stacking of trilayer graphene.

Here we derive band structure of ABA-stacked trilayer graphene. Considering the nearest neighbor hopping, tight-binding Hamiltonian is written as

$$H_{ABA} = \hbar v_F \begin{pmatrix} 0 & \tau k_x - i k_y & 0 & 0 & 0 & 0 \\ \tau k_x + i k_y & 0 & \gamma & 0 & 0 & 0 \\ 0 & \gamma & 0 & \tau k_x - i k_y & \gamma & 0 \\ 0 & 0 & \tau k_x + i k_y & 0 & 0 & 0 \\ 0 & 0 & \gamma & 0 & 0 & \tau k_x + i k_y \\ 0 & 0 & 0 & 0 & \tau k_x - i k_y & 0 \end{pmatrix}, \quad (2.27)$$

where the basis is defined by A1, B1, A2, B2, A3, and B3 atoms (Fig. 2.6).

Performing an unitary transformation to change the basis to $|A2\rangle$, $|B2\rangle$, $1/\sqrt{2}(|A1\rangle - |A3\rangle)$, $1/\sqrt{2}(|B1\rangle - |B3\rangle)$, $1/\sqrt{2}(|A1\rangle + |A3\rangle)$, and $1/\sqrt{2}(|B1\rangle + |B3\rangle)$, the Hamiltonian is written as

$$\tilde{H}_{ABA} = \begin{pmatrix} H_{ML} & 0 \\ 0 & H_{BL} \end{pmatrix}, \quad (2.28)$$

where

$$H_{ML} = \hbar v_F \begin{pmatrix} 0 & \tau k_x + i k_y \\ \tau k_x - i k_y & 0 \end{pmatrix} \quad (2.29)$$

and

$$H_{BL} = \hbar v_F \begin{pmatrix} 0 & \tau k_x + i k_y & 0 & 0 \\ \tau k_x - i k_y & 0 & \gamma & 0 \\ 0 & \gamma & 0 & \tau k_x + i k_y \\ 0 & 0 & \tau k_x - i k_y & 0 \end{pmatrix}. \quad (2.30)$$

Since Eq. 2.29 and 2.30 are equivalent with the tight-binding Hamiltonian of monolayer graphene and bilayer graphene, band structure of ABA-stacked trilayer graphene is expressed by the sum of monolayer graphene-like linear band and bilayer graphene-like parabolic band. In this tight binding model with only nearest neighbor hopping, monolayer-like band and bilayer-like band have band touching point at zero energy, however, calculation with further hoppings results in gap opening of both bands and positive shift of monolayer-like band [1,2] (Fig. 2.7).

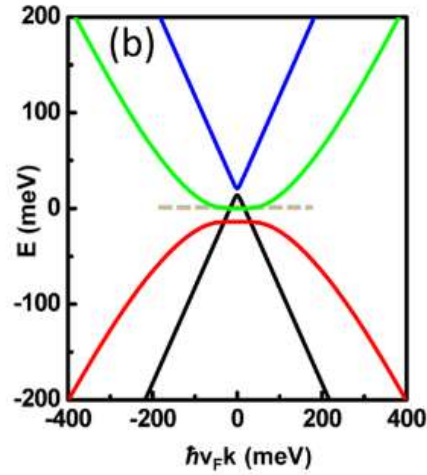


Figure 2.7: Band structure of ABA-stacking calculated by tight-binding model [2].

2.2 Quantum Hall effect of graphene

In this section, Landau quantization of monolayer graphene and bilayer graphene is discussed in the one-particle picture. Electron correlation effect will be discussed later in Chapter 4.

2.2.1 Two-dimensional free electron gas

Before thinking about graphene, we briefly derive the Landau quantization of conventional two-dimensional free electron gas. Hamiltonian for application of an out-of-plane magnetic field B is expressed as

$$\begin{aligned} H &= \frac{(\mathbf{p} + e\mathbf{A})^2}{2m} \\ &= \frac{p_x^2}{2m} + \frac{(p_y + eBx)^2}{2m}, \end{aligned} \quad (2.31)$$

where, we choose the Landau gauge $\mathbf{A} = (0, eBx, 0)$.

Assuming the eigenstate in the form of $\psi = \exp(ik_y y)\psi(x)$, Schrodinger equation is

$$\begin{aligned} \left[\frac{p_x^2}{2m} + \frac{(p_y + eBx)^2}{2m} \right] \exp(ik_x x)\psi(y) &= E \exp(ik_y y)\psi(x) \\ \left[\frac{p_x^2}{2m} + \frac{(\hbar k_y + eBx)^2}{2m} \right] \psi(x) &= E\psi(x). \end{aligned} \quad (2.32)$$

Left side of Eq. 2.32 is the Hamiltonian for an electron in harmonic potential centered at $-\hbar k_y/eB$, whose eigenenergy is

$$E_N = \frac{\hbar eB(N + \frac{1}{2})}{m} = \hbar\omega_c(N + \frac{1}{2}), \quad N = 0, 1, 2, \dots \quad (2.33)$$

where, ω_c is called cyclotron frequency. This quantization of energy under a out-of-plane magnetic field is called Landau quantization.

Next, we consider degeneracy of each Landau levels (LLs). Since ψ_x has one-to-one correspondence with k_y , we can know the degeneracy by counting up the number of possible k_y . Now we suppose a finite size system with length of L_x and L_y , considering periodic boundary condition,

$$k_y = \frac{2\pi}{L_y}m \quad (2.34)$$

with integer m .

On the other hand, harmonic potential centered at $-\frac{\hbar k_y}{eB}$ leads to

$$0 \leq \frac{\hbar k_y}{eB} \leq L_x. \quad (2.35)$$

Combining Eq. 2.34 and Eq. 2.35, we obtain

$$0 \leq m \leq \frac{eBL_xL_y}{h} = \frac{BL_xL_y}{\Phi_0}. \quad (2.36)$$

Here, $\Phi_0 = h/e$ is called quantized magnetic flux.

The degeneracy of Landau levels is the same with the number of quantized magnetic flux penetrating the system.

2.2.2 Monolayer graphene

Monolayer graphene is different from the conventional two-dimensional free electron gas in terms of the existence of two sublattices, zero gap between the conduction and valence band, and linear band dispersion. These differences lead to unique features of the quantum Hall effect in monolayer graphene.

By applying a perpendicular magnetic field and in the effective mass approximation ($\hbar\mathbf{k} = \mathbf{p}$) of Eq. 2.10, we obtain Hamiltonian

$$H = \begin{pmatrix} \Delta & v_F [\tau p_x - i(p_y + eBx)] \\ v_F [\tau p_x + i(p_y + eBx)] & -\Delta \end{pmatrix}. \quad (2.37)$$

In K valley ($\tau = 1$), using a new creation operator π^\dagger defined as

$$\pi^\dagger = \frac{1}{\sqrt{2\hbar eB}} [p_x - i(p_y + eBx)], \quad (2.38)$$

we can rewrite Eq. 2.37 as

$$H = v_F \sqrt{2\hbar eB} \begin{pmatrix} \frac{\Delta}{v_F \sqrt{2\hbar eB}} & \pi^\dagger \\ \pi & -\frac{\Delta}{v_F \sqrt{2\hbar eB}} \end{pmatrix}. \quad (2.39)$$

Since the new creation and annihilation operators meet the commutation relation

$$\begin{aligned} [\pi, \pi^\dagger] &= -\frac{1}{\hbar} [p_x, x] \\ &= 1, \end{aligned} \quad (2.40)$$

eigenenergies and eigenstates of $\pi\pi^\dagger$ have the following relations,

$$\pi\pi^\dagger |N\rangle = N |N\rangle \quad (2.41)$$

$$\pi^\dagger |N\rangle = \sqrt{N+1} |N+1\rangle \quad (2.42)$$

$$\pi |N\rangle = \sqrt{N} |N-1\rangle \quad (N \geq 1) \quad (2.43)$$

$$\pi |0\rangle = 0. \quad (2.44)$$

Therefore eigenenergies and eigenstates of H are expressed in the form of

$$|\psi_N\rangle = \begin{pmatrix} \alpha |N\rangle \\ \beta |N-1\rangle \end{pmatrix} \quad (N \geq 1) \quad (2.45)$$

$$|\psi_0\rangle = \begin{pmatrix} |0\rangle \\ 0 \end{pmatrix}, \quad (2.46)$$

here α , β , and E_N ($N \geq 2$) hold the relation

$$v_F \sqrt{2\hbar e B} \begin{pmatrix} \frac{\Delta}{v_F \sqrt{2\hbar e B}} & \frac{\sqrt{N}}{\sqrt{N}} \\ -\frac{\Delta}{v_F \sqrt{2\hbar e B}} & \end{pmatrix} \begin{pmatrix} \alpha \\ \beta \end{pmatrix} = E_N \begin{pmatrix} \alpha \\ \beta \end{pmatrix}, \quad (2.47)$$

which leads to the eigenenergies of

$$E_N = \sqrt{2\hbar v_F^2 e B N + \Delta^2} \quad (2.48)$$

On the other hand, in K' valley ($\tau = -1$), using

$$\pi^\dagger = -\frac{1}{\sqrt{2\hbar e B}} [p_x - i(p_y + e B x)], \quad (2.49)$$

Hamiltonian is written as

$$H = v_F \sqrt{2\hbar e B} \begin{pmatrix} \frac{\Delta}{v_F \sqrt{2\hbar e B}} & \pi \\ \pi^\dagger & -\frac{\Delta}{v_F \sqrt{2\hbar e B}} \end{pmatrix}. \quad (2.50)$$

Therefore using the same α and β determined by Eq. 2.47, eigenenergies and eigenstates are derived as following,

$$|\psi_N\rangle = \begin{pmatrix} \beta |N-1\rangle \\ \alpha |N\rangle \end{pmatrix} \quad (N \geq 1) \quad (2.51)$$

$$|\psi_0\rangle = \begin{pmatrix} 0 \\ |0\rangle \end{pmatrix} \quad (2.52)$$

$$E_N = \sqrt{2\hbar v_F^2 e B N + \Delta^2}. \quad (2.53)$$

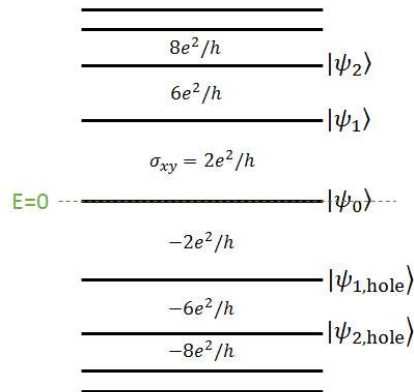


Figure 2.8: Landau levels of monolayer graphene.

Schematic of the Landau levels are shown in Fig. 2.8. There are two important differences between LLs in conventional free electron gas and those in monolayer graphene. One is that the LLs are proportional to \sqrt{NB} in monolayer graphene, while they are proportional to NB in free electron gas. The other is the existence of a LL at zero energy (zeroth Landau level; zLL) in monolayer graphene, whose wave function is localized in A (B) site for K (K') valley.

The former is naively explained by linear band dispersion in monolayer graphene. LLs have the degeneracy of $\Phi \propto B$ per one electron internal DOF both in graphene and free electron gas.

For a parabolic band structure, number of states $\Omega(E)$ below energy E is proportional to $k^2 \propto E$. When a magnetic field is applied, the number of LLs below the energy E should be $\Omega(E)/\Phi \propto E/B$. This lead to the LLs energy of $E_N \propto NB$.

On the other hand, for a linear band structure, number of states $\Omega(E)$ is proportional to $k^2 \propto E^2$, which leads to the LL's energy of $E_N \propto \sqrt{NB}$.

The later, existence of zLL is associated with the existence of two sublattices in monolayer graphene. Actually the zLL also appears in bilayer graphene which also has two sublattices.

2.2.3 Bilayer graphene

By applying a magnetic field and using the effective mass approximation ($\hbar\mathbf{k} = \mathbf{p}$) in Eq. 2.24, we obtain a Hamiltonian for bilayer graphene,

$$\begin{aligned} H_{2L} &= \frac{v_F^2}{\gamma} \begin{pmatrix} \frac{\gamma\Delta}{v_F^2} & [\tau p_x - i(p_y + eBx)]^2 \\ [\tau p_x + i(p_y + eBx)]^2 & -\frac{\gamma\Delta}{v_F^2} \end{pmatrix} \\ &= \frac{2v_F^2\hbar eB}{\gamma} \begin{pmatrix} \frac{\gamma\Delta}{2v_F^2\hbar eB} & (\pi^\dagger)^2 \\ \pi^2 & -\frac{\gamma\Delta}{2v_F^2\hbar eB} \end{pmatrix}, \end{aligned} \quad (2.54)$$

where π^\dagger and π are defined by Eq. 2.38.

Eigenstates of this Hamiltonian take the forms of

$$|\psi_N\rangle = \begin{pmatrix} \alpha |N\rangle \\ \beta |N-2\rangle \end{pmatrix} \quad (N \geq 2) \quad (2.55)$$

$$|\psi_1\rangle = \begin{pmatrix} |1\rangle \\ 0 \end{pmatrix} \quad (2.56)$$

$$|\psi_0\rangle = \begin{pmatrix} |0\rangle \\ 0 \end{pmatrix} \quad (2.57)$$

$$\cdot \quad (2.58)$$

Since α , β and E_N ($N \geq 2$) hold the relations

$$\frac{2v_F\hbar eB}{\gamma} \begin{pmatrix} \frac{\gamma\Delta}{2v_F\hbar eB} & \sqrt{N(N-1)} \\ \sqrt{N(N-1)} & -\frac{\gamma\Delta}{2v_F\hbar eB} \end{pmatrix} \begin{pmatrix} \alpha \\ \beta \end{pmatrix} = E_N \begin{pmatrix} \alpha \\ \beta \end{pmatrix}, \quad (2.59)$$

eigenenergies are derived as

$$E_N = \sqrt{(2v_F\hbar eB/\gamma)^2 N(N-1) + \Delta^2} \quad (N \geq 2) \quad (2.60)$$

$$E_1 = E_0 = \Delta. \quad (2.61)$$

Different from that in monolayer graphene, E_N in bilayer graphene is proportional to NB reflecting its parabolic band dispersion (Fig. 2.9). In addition, $|\psi\rangle_1$ and $|\psi\rangle_0$ are degenerated at zero energy. Therefore, considering the spin and valley, zLL of bilayer graphene has 8-fold degeneracy.

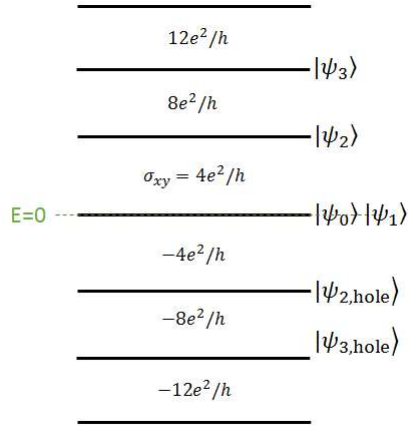


Figure 2.9: Schematic of LLs in bilayer graphene.

Chapter 3

Charge neutral currents in graphene

Flow of internal degrees of freedom of electrons, such as spin and valley, are promising for future low-power devices because such charge neutral currents that do not accompany electric current are much less dissipative than electric current. In this chapter two streams of previous researches to utilize charge neutral current in graphene are introduced, towards graphene-based spintronics and valleytronics.

3.1 Spintronics in graphene

3.1.1 Spin current injection and transport

Spintronics is a technology to utilize the spin DOF for electric device such as information storages, logic devices, and information transmission devices. To realize it, realization of a spin transport channel with less scattering, and generation and detection of the spin current there are main challenges. For the former graphene is a good material, because small spin-orbit interaction (SOI) makes its spin diffusion length longer than other semiconductor materials. In this subsection, we describe researches on spin current injection and propagation in graphene.

To inject spin current from ferromagnetic metal to graphene, ‘nonlocal’ geometry (Fig. 3.1) is usually used. Current is applied between electrode 1 and ferromagnetic electrode 2. Difference of spin polarization between electrodes 1 and 2 generates spin accumulation under these electrodes. Accumulated spin diffuses and creates the spin voltage, which is defined by the difference of chemical potential between opposite spins. Spin voltage is detected as a voltage between ferromagnetic electrode 3 and electrode 4. The ratio of injected current between electrode 1 and 2, and measured voltage between electrode 3 and 4 is called nonlocal resistance.

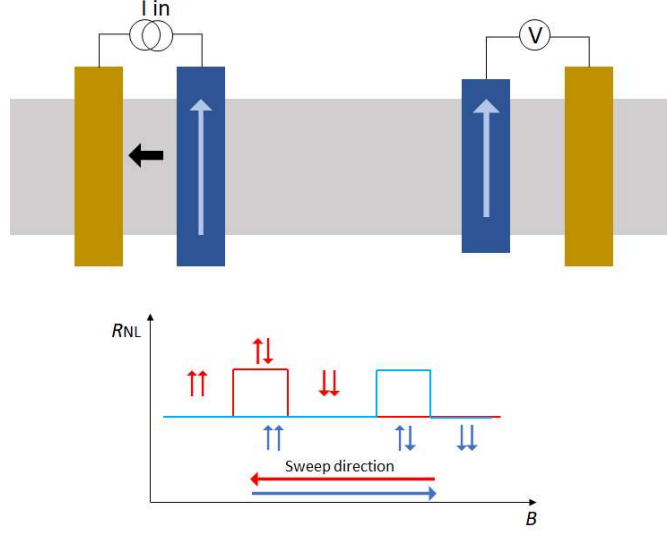


Figure 3.1: Schematic of spin injection in nonlocal geometry.

Spin injection to graphene was first realised in monolayer graphene on SiO_2 substrate using Cobalt electrodes [3,4](Fig. 3.2). Spin diffusion length of $1.5 \mu\text{m}$ was reported at room temperature. By encapsulating graphene between hexagonal boron nitride, spin diffusion length was dramatically increased up to $30 \mu\text{m}$ [5]. Such a long spin diffusion length is due to the weakness of SOI which causes spin relaxation. However, spin diffusion length of dozens of microns is two orders of magnitude smaller than that expected from theoretical prediction [6], assuming the spin-orbit interaction of $12 \mu\text{eV}$ in monolayer graphene as a cause of spin relaxation. This discrepancy indicates that the spin relaxation is mainly caused by extrinsic origins in graphene, such as impurities, substrate, defects, ripples, and nuclear spins.

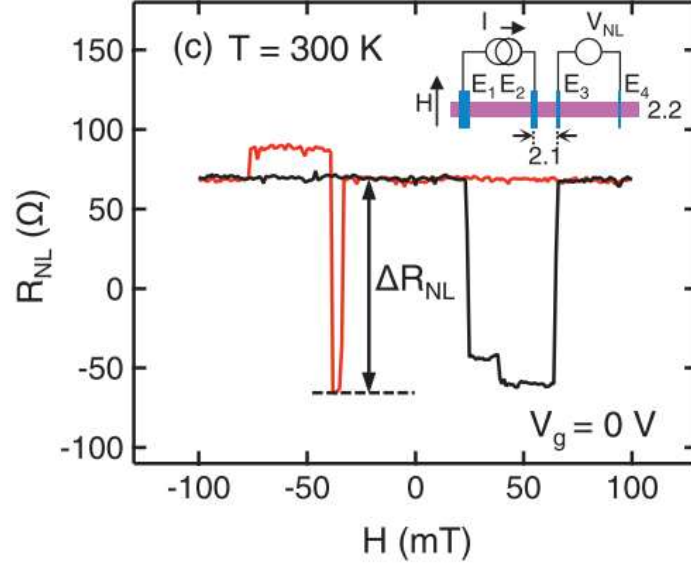


Figure 3.2: Tunneling spin injection and detection using Co electrode on monolayer graphene through TiO_2 insulating layer [4]. The black (red) curve shows the nonlocal resistance as the magnetic field is swept up (down). Inset: Schematic of nonlocal spin transport measurement.

Although the primary origin of spin relaxation is still controversial, some experiments suggest negligible contribution of nuclear spins [7]. One experiment suggests the atomic defects which act as a magnetic moment as a main origin of spin relaxation [8].

Weak SOI of μeV order in graphene is usually experimentally undetectable, however, it was recently detected in bilayer graphene as a small difference of lifetime between out-of-plane-polarized spin and in-plane-polarized spin [9]. Since spin-orbit interaction acts as an out-of-plane effective magnetic field, it relaxes in-plane-polarized spin more than out-of-plane-polarized spin, when the Fermi energy is tuned to be zero. They measured dual-gate dependence of spin lifetime anisotropy and found that the anisotropy significantly increases at zero carrier density (Fig. 3.3).

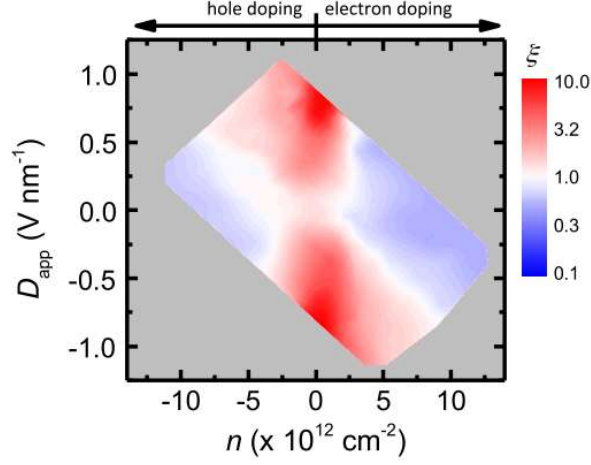


Figure 3.3: Displacement field D_{app} and carrier density n dependence of anisotropy of spin lifetime ξ obtained from its top gate and back gate dependence [9].

3.1.2 Spin Hall effect

Spin Hall effect is a spin dependent Hall effect caused by opposite sign of Hall conductivity for opposite spins. This effect enables the conversion between charge current (or voltage) and spin current (or spin voltage) without any external structure such as ferromagnetic electrodes, therefore is one of the most important technological ingredient in spintronics. The mechanism of spin Hall effect is categorized into two, extrinsic and intrinsic mechanism. Extrinsic mechanism arises from spin dependent scattering caused by SOI around impurities and intrinsic mechanism arises from spin dependent pseudo-magnetic field caused by bending of band structure due to SOI. Origins of both mechanisms are spin-orbit interaction.

When we consider monolayer graphene with electron interaction energy, temperature, and Fermi energy fluctuation smaller than its spin-orbit energy, we can expect intrinsic spin Hall effect as theoretically proposed in [10]. Although this proposal is important as the first theoretical discovery of graphene as a topological insulator, the situation is unrealistic in graphene owing not only to the constraint of temperature and fluctuation but also to much stronger electron interaction than spin-orbit interaction. Therefore we cannot observe intrinsic spin Hall effect in graphene, instead, we can introduce spin-orbit interaction externally using substrate, adatoms, and nanoparticles with strong spin-orbit interaction and observe extrinsic spin Hall effect.

Decoration of hydrogen atoms induces the deformation of carbon bond and brings the σ bond electrons into the π bond, which compose the conduction and valence band of graphene. Since the σ state has SOI of around 10 meV, this deformation of bond enhances the spin-orbit interaction of conductive electrons. Spin Hall effect has been observed using ‘nonlocal resistance measurement’ in a Hall bar sample of hydrogenated graphene [11].

Spin Hall effect induced by adatoms is also observed in monolayer graphene grown by chemical vapor deposition (CVD). Since copper is used as a growth substrate, copper atoms are

naturally stick to the graphene surface and introduce SOI [12]. In monolayer graphene decorated by Bi_2Te_3 nanoparticles, larger spin Hall conductivity and signature of quantization is observed due to the strong SOI in Bi_2Te_3 [13]. Fig. 3.4 shows the schematic of the nonlocal

resistance measurement and measured nonlocal resistance [12]. Nonlocal resistance measurement is a widely used technique to confirm the existence of charge neutral current generated via a Hall effect. They inject current between the left two terminals of the Hall bar, which generates spin current in the longitudinal direction of the Hall bar via spin Hall effect. Spin current propagates over few microns due to its non-dissipative property, and is detected as a voltage between the right two terminals via inverse spin Hall effect (Fig. 3.4(a)). Fig. 3.4(b) shows the nonlocal resistance in CVD-grown monolayer graphene (red curve in upper panel), that in pristine monolayer graphene (red curve in lower panel). Estimated nonlocal resistance due to trivial Ohmic current diffusion (see Chapter 5 for detail) is indicated by gray broken curves. We can see that nonlocal resistance much larger than the trivial current diffusion contribution is observed in CVD-grown monolayer graphene decorated by copper atoms, indicating the existence of spin current generated via spin Hall effect.

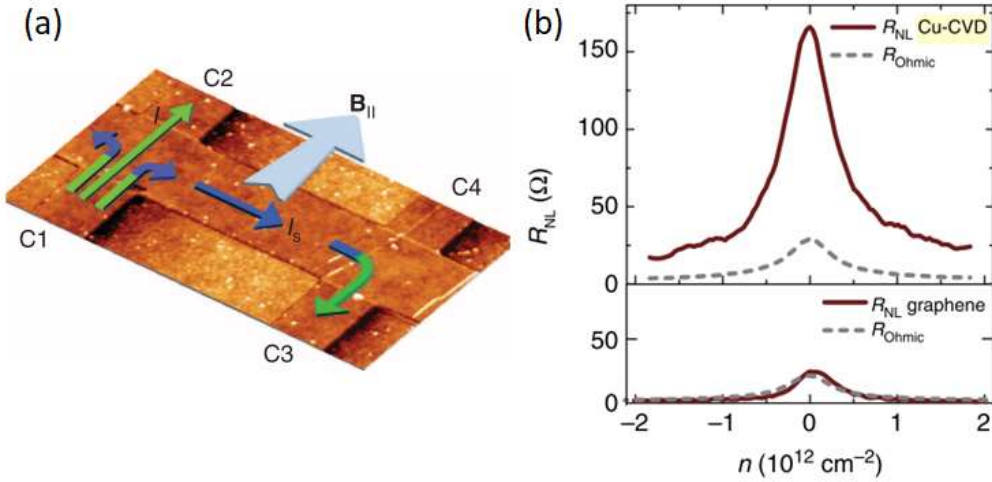


Figure 3.4: Schematic of nonlocal resistance measurement (a) and measured nonlocal resistance (b) [12].

(a) Green (blue) arrows indicate charge (spin) current. (b) Nonlocal resistance in CVD-grown monolayer graphene and normal monolayer graphene are shown as the red curves in upper and lower panels, respectively. Gray broken curves are Ohmic contribution of nonlocal resistance, whose detail is explained in Chapter 5.

Spin Hall effect is also observed in monolayer graphene stacked on substrates with strong SOI such as transition metal dichalcogenides [14].

3.2 Valleytronics in graphene

3.2.1 Berry curvature

Berry curvature is the curvature of wave function in momentum space or any other parameter space, and is the origin of valley Hall effect. To derive the Berry curvature, we first introduce Berry phase.

Here we consider a Hamiltonian $H(\mathbf{R})$ which contain a parameter \mathbf{R} . Its eigenenergies and eigenstates are written as

$$H(\mathbf{R}) |\phi_n(\mathbf{R})\rangle = E_n(\mathbf{R}) |\phi_n(\mathbf{R})\rangle, \quad (3.1)$$

where n is the index of the eigenenergy and eigenstate.

We consider an adiabatic time evolution of arbitrary state $|\Phi(t)\rangle$ associated with the time evolution of parameter $\mathbf{R}(t)$, which is described by the time-dependent Schrodinger equation,

$$i\hbar \frac{\partial}{\partial t} |\Phi(t)\rangle = H(\mathbf{R}(t)) |\Phi(t)\rangle. \quad (3.2)$$

If the initial state is n -th eigenstate $|\Phi(t=0)\rangle = |\phi_n(\mathbf{R}(t=0))\rangle$, the state remains to be n -th state according to the adiabatic theorem,

$$|\Phi(t)\rangle \propto |\phi_n(\mathbf{R}(t))\rangle. \quad (3.3)$$

The proportional coefficient of Eq. 3.3 can be arbitrary complex value of the absolute value 1, therefore,

$$|\Phi(t)\rangle = e^{i\theta(t)} |\phi_n(\mathbf{R}(t))\rangle. \quad (3.4)$$

By substituting Eq. 3.4 to Eq. 3.2 and taking the inner product with $\langle \phi_n(\mathbf{R}(t))|$, we obtain

$$\begin{aligned} \frac{d\theta(t)}{dt} &= -\frac{1}{\hbar} E_n(\mathbf{R}(t)) + i \langle \phi_n(\mathbf{R}(t)) | \frac{\partial}{\partial t} | \phi_n(\mathbf{R}(t)) \rangle \\ \theta(t) &= \frac{1}{\hbar} \int_0^t dt' E_n(\mathbf{R}(t')) + i \int_0^t dt' \langle \phi_n(\mathbf{R}(t')) | \frac{\partial}{\partial t'} | \phi_n(\mathbf{R}(t')) \rangle. \end{aligned} \quad (3.5)$$

The first term of Eq. 3.5 is the oscillation in the frequency proportional to the energy, and become nonzero even if there is no change of \mathbf{R} . This is called dynamical phase.

The second term is originated from the time evolution of \mathbf{R} , and is called Berry phase. We will represent this Berry phase as $\gamma(t)$.

When the time evolution of \mathbf{R} takes a closed-path $\mathbf{R}(t=0) = \mathbf{R}(t=T)$, Berry phase can be deformed as

$$\gamma(T) = i \int_0^T dt' \langle \phi_n(\mathbf{R}(t')) | \frac{\partial}{\partial t'} | \phi_n(\mathbf{R}(t')) \rangle \quad (3.6)$$

$$= \oint_C d\mathbf{R} \cdot i \langle \phi_n(\mathbf{R}) | \frac{\partial}{\partial \mathbf{R}} | \phi_n(\mathbf{R}) \rangle \quad (3.7)$$

$$= \int_S d\mathbf{S} \cdot \nabla_{\mathbf{R}} \times i \langle \phi_n(\mathbf{R}) | \frac{\partial}{\partial \mathbf{R}} | \phi_n(\mathbf{R}) \rangle \quad (3.8)$$

$$= \int_S d\mathbf{S} \cdot \mathbf{\Omega}_n(\mathbf{R}). \quad (3.9)$$

Here,

$$\mathbf{\Omega}_n(\mathbf{R}) \equiv \nabla_{\mathbf{R}} \times i \langle \phi_n(\mathbf{R}) | \frac{\partial}{\partial \mathbf{R}} | \phi_n(\mathbf{R}) \rangle \quad (3.10)$$

is called Berry curvature, C is the closed-path of $\mathbf{R}(t)$, and S is the region inside the closed-path.

We can see that Berry phase does not depend on the detail of time evolution, but is determined by the surface integral of Berry curvature over a parameter space penetrating the parameter closed-path. Therefore the relation between Berry phase and Berry curvature has analogy with the relation between Aharonov-Born phase and real-space magnetic field. That's why Berry curvature is considered to be pseudo-magnetic field in the parameter space. Below, parameter space of Berry curvature is the momentum space if not specified.

To derive the relationship between Berry curvature and Hall conductivity, we deform the expression of Berry curvature in Eq. 3.10.

$$\begin{aligned} \mathbf{\Omega}_n(\mathbf{k}) &= i \nabla_{\mathbf{k}} \times \left\langle \phi_n(\mathbf{k}) \left| \frac{\partial}{\partial \mathbf{k}} \right| \phi_n(\mathbf{k}) \right\rangle \\ &= i \left(\frac{\partial}{\partial k_x}, \frac{\partial}{\partial k_y}, \frac{\partial}{\partial k_z} \right) \times \\ &\quad \left(\left\langle \phi_n(\mathbf{k}) \left| \frac{\partial}{\partial k_x} \right| \phi_n(\mathbf{k}) \right\rangle, \left\langle \phi_n(\mathbf{k}) \left| \frac{\partial}{\partial k_y} \right| \phi_n(\mathbf{k}) \right\rangle, \left\langle \phi_n(\mathbf{k}) \left| \frac{\partial}{\partial k_z} \right| \phi_n(\mathbf{k}) \right\rangle \right) \\ &= i \left\langle \frac{\partial \phi_n}{\partial \mathbf{k}} \right| \times \left| \frac{\partial \phi_n}{\partial \mathbf{k}} \right\rangle \\ &= i \sum_m \left\langle \frac{\partial \phi_n}{\partial \mathbf{k}} \right| \phi_m \rangle \times \left\langle \phi_m \left| \frac{\partial \phi_n}{\partial \mathbf{k}} \right\rangle \right. \\ &= i \sum_{m(\neq n)} \frac{\langle \phi_n | \frac{\partial H}{\partial \mathbf{k}} | \phi_m \rangle \times \langle \phi_m | \frac{\partial H}{\partial \mathbf{k}} | \phi_n \rangle}{(E_n - E_m)^2}, \end{aligned} \quad (3.11)$$

here, n and m are band indices and we used the relation

$$\left\langle \phi_m \left| \frac{\partial \phi_n}{\partial k_j} \right\rangle = \frac{1}{E_n - E_m} \left\langle \phi_m \left| \frac{\partial H}{\partial k_j} \right| \phi_n \right\rangle \quad (3.12)$$

for the last deformation. We can see that large Berry curvature appear near the band crossing where $E_n - E_m$ becomes small.

Then we consider the Hall conductivity in the context of linear response theory. When electric field is applied in parallel to x-axis, wave function of n-th band is deformed as

$$|nk'\rangle = |nk\rangle - eE \sum_{m(\neq n)} \frac{\langle mk | x | nk \rangle}{\epsilon_n(k) - \epsilon_m(k)} |mk\rangle. \quad (3.13)$$

Now, current density for this deformed wave function is

$$\langle j \rangle' = \sum_{n,k} \left[\langle nk | j | nk \rangle - eE \sum_{m(\neq n),k} \frac{\langle nk | j | mk \rangle \langle mk | x | nk \rangle}{\epsilon_n(k) - \epsilon_m(k)} + c.c \right]. \quad (3.14)$$

Since the first term is the current density without electric field which should be zero, the second term is important.

Here, taking the matrix elements of the general relationship between current operator and polarization operator

$$j = \frac{dP}{dt} = \frac{1}{i\hbar} [P, H], \quad (3.15)$$

we obtain

$$\begin{aligned} \langle mk | j | nk \rangle &= \frac{1}{i\hbar} \langle mk | [P, H] | nk \rangle \\ &= \frac{1}{i\hbar} \langle mk | [P\epsilon_n(k) - \epsilon_m(k)P] | nk \rangle \\ &= \frac{1}{i\hbar} (\epsilon_n(k) - \epsilon_m(k)) \langle nk | P | mk \rangle. \end{aligned} \quad (3.16)$$

By substituting Eq. 3.16 into Eq. 3.14, current density along $\alpha = x$ or y axis is written as

$$\langle j_\alpha \rangle' = \frac{1}{i\hbar} \left[\sum_{m,k} \frac{\langle nk | j_\alpha | mk \rangle \langle mk | j_\alpha | nk \rangle}{(\epsilon_n(k) - \epsilon_m(k))^2} E + c.c \right]. \quad (3.17)$$

By substituting relation between canonically conjugate operators

$$j_\alpha = \frac{\partial H}{\partial k_\alpha} \quad (3.18)$$

into Eq. 3.17, we obtain following expression

$$\langle j_\alpha \rangle' = \frac{1}{i\hbar} \left[\sum_{m,k} \frac{\langle nk | \frac{\partial H}{\partial k_\alpha} | mk \rangle \langle mk | \frac{\partial H}{\partial k_\alpha} | nk \rangle}{(\epsilon_n(k) - \epsilon_m(k))^2} E + c.c \right]. \quad (3.19)$$

Using Eq. 3.11,

$$\langle j_y \rangle' = -\frac{e^2}{h} \sum_n \int_{BZ} \frac{d^2k}{2\pi} \Omega_{n,z}(\mathbf{k}) \times E, \quad (3.20)$$

therefore the Hall conductivity is written by integral of Berry curvature over the Brillouin zone as following.

$$\sigma_{xy} = -\frac{e^2}{h} \sum_n \int_{BZ} \frac{d^2k}{2\pi} \Omega_{n,z}(\mathbf{k}) \quad (3.21)$$

3.2.2 Valley Hall effect

Next we calculate Berry curvature in graphene and derive valley Hall effect. Generally, Hamiltonian of a following shape,

$$H(\mathbf{R}) = \mathbf{R} \cdot \boldsymbol{\sigma}, \quad \mathbf{R} = R(\sin \theta \cos \phi, \sin \theta \sin \phi, \cos \theta) \quad (3.22)$$

has eigenenergies and eigenstates of

$$E = \pm R, \quad \psi = \begin{pmatrix} \cos \frac{\phi}{2} \\ \pm e^{i\theta} \sin \frac{\phi}{2} \end{pmatrix}. \quad (3.23)$$

Based on the definition of

$$\mathbf{A} = i \langle \psi(\mathbf{R}) | \nabla_{\mathbf{R}} | \psi(\mathbf{R}) \rangle, \quad \boldsymbol{\Omega} = \nabla_{\mathbf{R}} \times \mathbf{A}, \quad (3.24)$$

z component of Berry curvature is calculated as

$$\Omega(\mathbf{k}) = \frac{\mathbf{R}}{2R^2} \cdot \left(\frac{\partial \mathbf{R}}{\partial R_x} \times \frac{\partial \mathbf{R}}{\partial R_y} \right). \quad (3.25)$$

Here we rewrite the low energy effective Hamiltonian in monolayer graphene (Eq. 2.10),

$$H = \hbar v_F (\tau k_x \sigma_x + k_y \sigma_y) + \Delta \sigma_z, \quad (3.26)$$

here, τ is the valley index and 2Δ is the energy difference between the two sublattices. This is the case of Eq. 3.22 with

$$\mathbf{R} = \hbar v_F (\tau k_x, k_y, \Delta/\hbar v_F), \quad (3.27)$$

therefore z component of Berry curvature is

$$\begin{aligned} \Omega(\mathbf{k}) &= \frac{(\tau k_x, k_y, \Delta/\hbar v_F)}{2(k_x^2 + k_y^2 + (\Delta/\hbar v_F)^2)^{\frac{3}{2}}} \cdot (0, 0, 1) \\ &= \frac{\tau \Delta/\hbar v_F}{2(k^2 + (\Delta/\hbar v_F)^2)^{\frac{3}{2}}} \\ &= \frac{\tau (\hbar v_F)^2 \Delta}{2(E_k^2 + \Delta^2)^{\frac{3}{2}}} \end{aligned} \quad (3.28)$$

Fig. 3.5 shows momentum space distribution of the z component of Berry curvature in the conduction band of monolayer graphene. Conduction band and valence band have opposite sign of Berry curvature, therefore they are cancel out when the energy gap is zero. Another important feature is that two valleys have opposite sign of Berry curvature. This lead to opposite sign of Hall conductivity for each valleys, which results in the valley Hall effect.

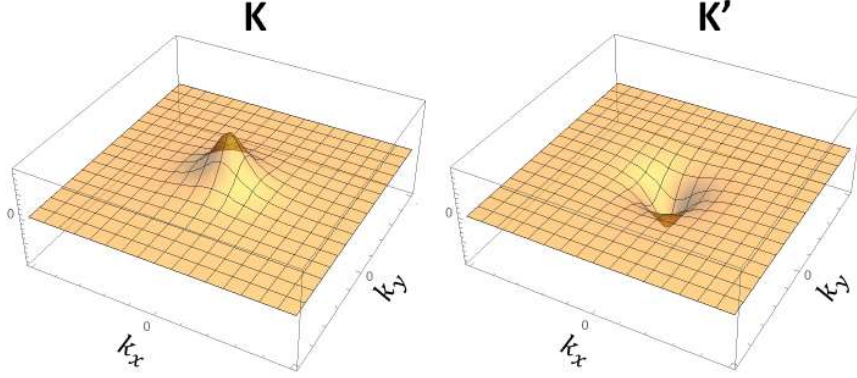


Figure 3.5: z component of Berry curvature in conduction band of monolayer graphene.

In bilayer graphene, similar calculation gives z component of the Berry curvature as following,

$$\Omega(\mathbf{k}) = \frac{2\tau(\hbar v_F)^2 E_k \Delta}{\gamma(E_k^2 + \Delta^2)^{\frac{3}{2}}}. \quad (3.29)$$

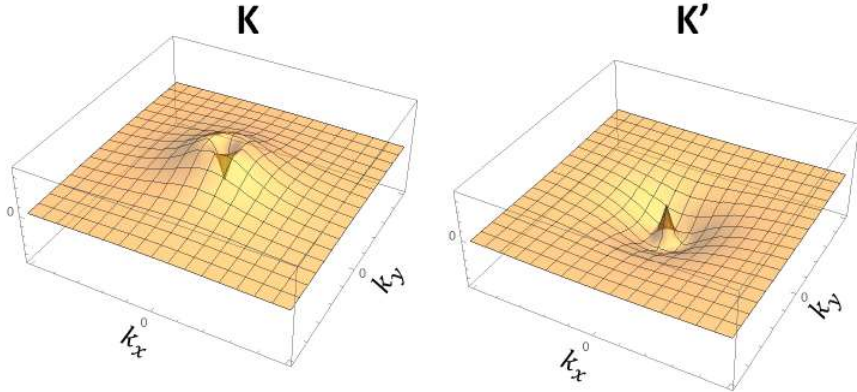


Figure 3.6: z component of Berry curvature in conduction band of bilayer graphene.

So far we derive the Berry curvature of monolayer and bilayer graphene. One important common feature is that they become non-zero only when energy gap opens, which is equivalent

to the inversion symmetry breaking. Another important feature is that they have opposite value in K and K' valley, which leads to the valley Hall effect.

According to Eq. 3.21, we can derive the valley dependent Hall conductivity by integrating Berry curvature for each valley. In monolayer graphene, it takes constant quantized value in the gap,

$$\begin{aligned}
\sigma_{xy,\tau} &= \tau \frac{2e^2}{\hbar} \frac{(\hbar v_F)^2 \Delta}{2\pi} \int_{-\infty}^0 dk \frac{k}{((\hbar v_F k)^2 + \Delta^2)^{\frac{3}{2}}} \\
&= \tau \frac{e^2}{h} (\hbar v_F)^2 \Delta \left[-\frac{1}{(\hbar v_F)^2 ((\hbar v_F k)^2 + \Delta^2)^{\frac{1}{2}}} \right]_{-\infty}^0 \\
&= -\tau \frac{e^2}{h},
\end{aligned} \tag{3.30}$$

and decreases as Fermi energy goes away from the gap,

$$\begin{aligned}
\sigma_{xy,\tau} &= \tau \frac{e^2}{h} (\hbar v_F)^2 \Delta \left[-\frac{1}{(\hbar v_F)^2 ((\hbar v_F k)^2 + \Delta^2)^{\frac{1}{2}}} \right]_{-\infty}^{-k} \\
&= -\tau \frac{e^2}{h} \frac{\Delta}{\sqrt{\epsilon_k^2 + \Delta^2}}.
\end{aligned} \tag{3.31}$$

Valley Hall conductivity is defined by

$$\sigma_{VH} \equiv \sigma_{xy,K} - \sigma_{xy,K'} = \frac{2e^2}{h} \frac{\Delta}{\sqrt{\epsilon_k^2 + \Delta^2}}. \tag{3.32}$$

In bilayer graphene, Hall conductivity is twice of that in monolayer graphene, reflecting the twice rotation of pseudospin around the Dirac points.

$$\sigma_{VH,2L} = \frac{4e^2}{h} \frac{\Delta}{\sqrt{\epsilon_{k,2L}^2 + \Delta^2}} \tag{3.33}$$

Valley Hall effect in graphene was first reported in monolayer graphene stacked on hexagonal boron nitride (h-BN) [15]. Lattice of h-BN introduces energy difference between the sublattices of monolayer graphene, which breaks the inversion symmetry and opens a energy gap at Dirac points. Similarly to previous researches of spin Hall effect, they perform non-local resistance measurement and observe large nonlocal resistance only in a angle-aligned h-BN/graphene stack.

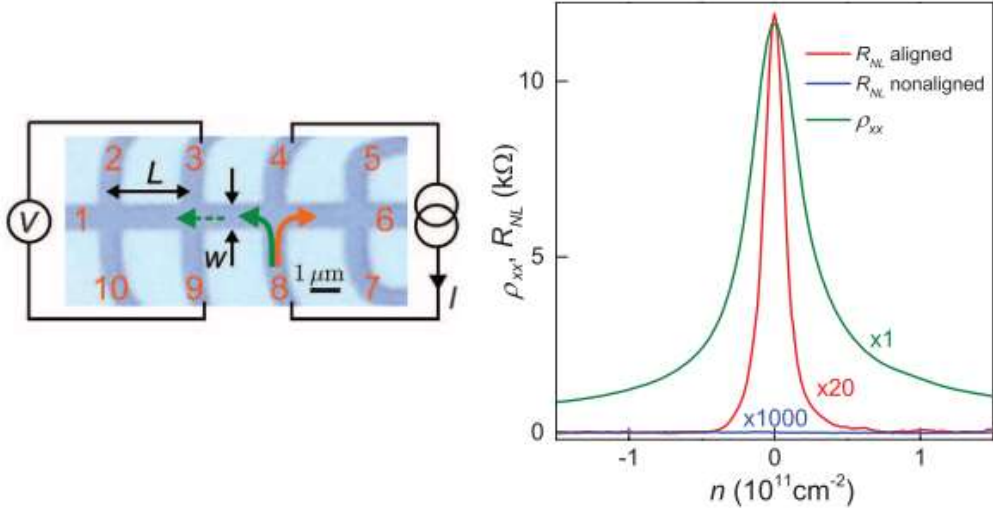


Figure 3.7: Optical microscope image of the Hall bar sample (left) and nonlocal resistance (right) [15]. In the right figure, nonlocal resistance in angle aligned monolayer graphene/h-BN stack and nonaligned stack are shown in red and blue curves, respectively. Green curve shows local resistivity.

After that, valley Hall effect was also observed in bilayer graphene [16,17]. Since energy gap of bilayer graphene can be controlled by out-of-plane electric field, they measure electric field dependence and temperature dependence of local and nonlocal resistance. They found cubic scaling dependence between the local and nonlocal resistances, which is the evidence that the nonlocal resistance is originated from valley current (Fig. 3.8).

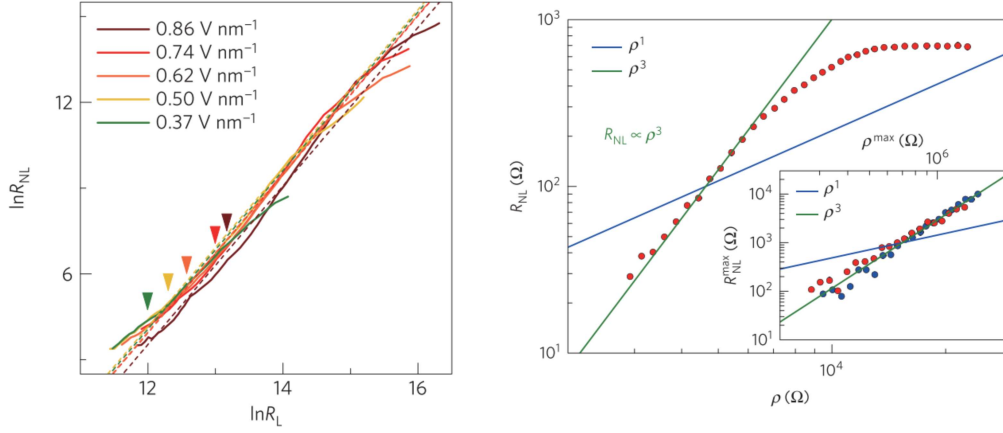


Figure 3.8: Scaling dependence of local and nonlocal resistance in valley Hall effect in [16](left) and [17](right). In the left figure, temperature is changed from 10 K to 300 K. Curves of different colors indicate the data in different out-of-plane electric field. In the right figure, temperature is fixed at 70 K and out-of-plane electric field is changed from 0.22 to 0.85 V/nm. Inset shows data from different samples.

In addition, the authors of [16] fabricated a Hall bar sample with a sticking-out region (Fig. 3.9), which makes the sample edge longer. They observe the same order of nonlocal resistance in the long edge sample and normal edge sample, which denies the possibility of edge transport as an origin of the nonlocal resistance.

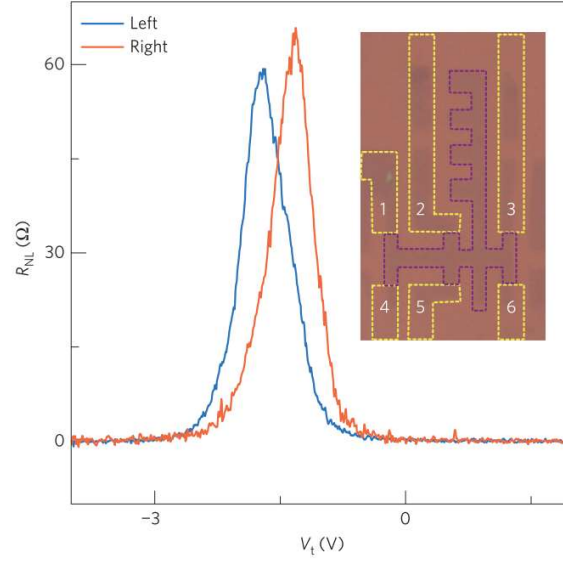


Figure 3.9: Nonlocal resistance in long edge sample and normal edge sample in valley Hall effect [16]. Sticking out region to make edge longer only exist on the right side of Hall bar. Current is applied between terminal 2 and 5, and nonlocal voltage is measured between terminal 1 and 4 (blue curve), and 3 and 6 (red curve).

Chapter 4

Quantum Hall ferromagnetism

4.1 Electron correlation energy v.s. Kinetic energy

Generally, Hamiltonian of an electronic system is composed of two parts, the kinetic energy and interaction energy. Relative dominance of these parts depends on the system. Since the kinetic energy is one-particle Hamiltonian, it is well solved and we can define the density of states (DOS). $1/\text{DOS}$ is the magnitude of the kinetic energy for one electron. On the other hand, interaction energy in electronic systems arises from Coulomb interaction, whose magnitude is $e^2/4\pi\epsilon l$ (ϵ and l are dielectric constant and distance between electrons, respectively). Relative dominance is determined by the competition of these two values.

Systems with large DOS have less kinetic energy, therefore interaction becomes relatively important. Such systems are called flat-band systems and include cuprates, Kagome magnets, and quantum Hall systems. These systems exhibit some common features. At half filling of the flat band, energy gap opens. In addition, this gap opening is accompanied by ordering of internal electron degrees of freedom due to exchange interaction.

In case of cuprates, the Mott insulating phase appears at half filling of the flat band composed of 3d orbital of copper. Here antiferromagnetic spin order appears owing to super exchange interaction.

In case of Kagome magnets, ferromagnetism is theoretically proved to be established due to macroscopic degeneracy, which is considered to be a complete flat band.

Quantum Hall states also have macroscopic degeneracy and exhibit gap opening and ordered state at the half filling of Landau levels. In following section, detail of quantum Hall magnetism is introduced.

4.2 Quantum Hall ferromagnetism

Here we first introduce the basic concept of quantum Hall ferromagnetism using a spin degenerated quantum Hall system as an example. As discussed in Chapter 2, one-particle theory of Landau quantization gives the discrete energy levels called Landau levels (LLs), which have degeneracy of BS/Φ_0 , where S is area of the sample and Φ_0 is the quantized magnetic flux (Eq. 2.36). Energy spacing between LLs is determined by the cyclotron energy $\hbar\omega_c = \frac{\hbar eB}{m^*}$ (Eq. 2.33). This energy is equal to Zeeman energy $\frac{g\hbar eB}{2m_e}$ in vacuum where the effective mass m^* is the same with bare electron mass m_e and g-factor g is 2. However, in a crystal, m^* is usually much smaller than m_e . In addition, crystals with large spin-orbit interaction such as GaAs have g-factor smaller than 2. Therefore Zeeman splitting is usually much smaller than the cyclotron energy and we can ignore Zeeman splitting and assume spin degenerated LLs. Here we consider half filling of a spin degenerated LL, where degeneracy of the LL is $2 \times BS/\Phi_0$ and electron occupation number is BS/Φ_0 . In a one-particle model, all filling orders have the equivalent energy (Fig. 4.1). However, when we introduce electron correlation, exchange energy favors one filling order, where only states of one spin are completely filled while others are empty (Fig. 4.1(c)). This is because of the positive exchange coupling between degenerated orbitals. According to the principle of quantum mechanics, degenerated orbitals are orthogonal with each other. Here we show that exchange integral between any orthogonal orbitals are positive.

Exchange integral J between orbitals $\phi_1(r)$ and $\phi_2(r)$ is defined as

$$J = \iint dr_1 dr_2 \phi_1^*(r_1) \phi_2^*(r_2) \frac{e^2}{4\pi\epsilon_0|r_1 - r_2|} \phi_2(r_2) \phi_1(r_1). \quad (4.1)$$

Eq. 4.1 is transformed into momentum space representation by Foulrier transformation $\frac{e^2}{|r_1 - r_2|} \rightarrow \frac{1}{\Omega} \sum_k \frac{4\pi e^2}{k^2} e^{i\mathbf{k} \cdot (r_1 - r_2)}$ as

$$\begin{aligned} J &= \frac{1}{\Omega} \sum_k \frac{4\pi e^2}{k^2} \iint dr_1 dr_2 \phi_1^*(r_1) \phi_2^*(r_2) e^{i\mathbf{k} \cdot (r_1 - r_2)} \phi_2(r_2) \phi_1(r_1) \\ &= \frac{1}{\Omega} \sum_k \frac{4\pi e^2}{k^2} \int dr_1 \phi_1^*(r_1) \phi_2(r_1) e^{i\mathbf{k} \cdot r_1} \int dr_2 \phi_1(r_2) \phi_2^*(r_2) e^{-i\mathbf{k} \cdot r_2}. \end{aligned} \quad (4.2)$$

Since integrals for r_1 and r_2 in Eq. 4.2 are conjugate with each other, J always becomes positive.

Therefore, exchange coupling between different orbitals in the same LLs is always positive and favors the ferromagnetic order.

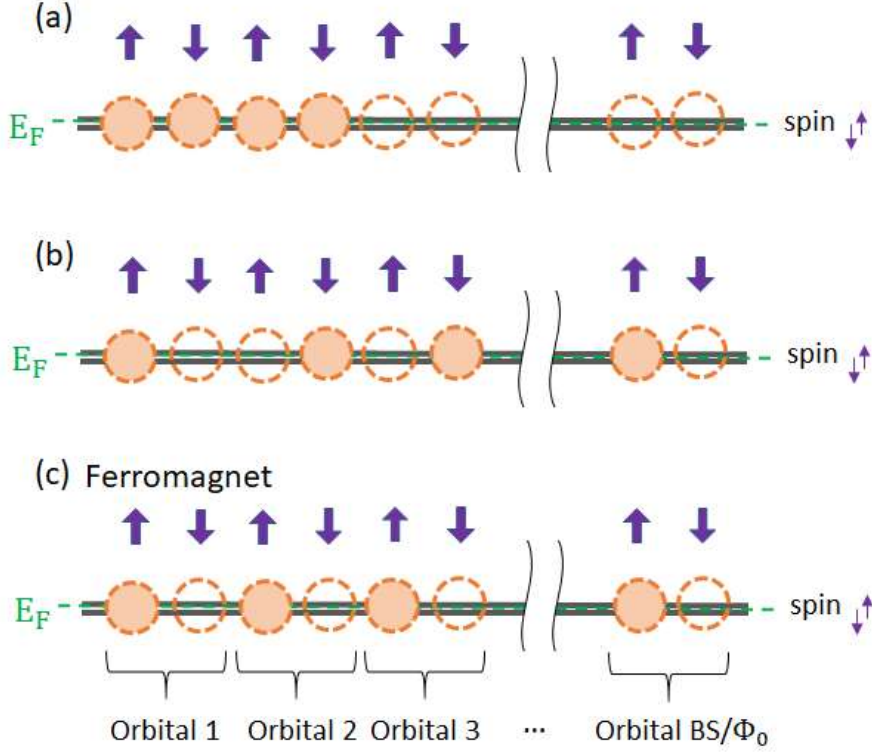


Figure 4.1: Occupation of electrons in a partially filled LL with spin degeneracy. Orbital 1, 2, 3, ... indicate BS/Φ_0 -fold degenerated orbitals with different angular momentum. (a), (b), and (c) are examples for different occupations. (a) and (b) are paramagnetic, and (c) is ferromagnetic occupation. In reality, (c) is realized due to the positive exchange energy between orbitals.

When ferromagnetic order is established, the system is stabilized by the exchange energy and energy gap opens, which leads to plateau in the Hall conductivity at odd integer filling ($\nu=1, 3, \dots$). This energy gap is of the same order with electron interaction energy $e^2/4\pi\epsilon l_B$. Here, $l_B = \sqrt{\hbar/eB}$ is the magnetic length, which is a typical distance between electrons in the quantum Hall state. The magnitude of interaction energy is

$$\begin{aligned}
 e^2/4\pi\epsilon l_B &\simeq 660 \frac{\sqrt{B[\text{T}]}}{\epsilon_r} [\text{K}] \\
 &\simeq 120 \sqrt{B[\text{T}]} [\text{K}] \quad (\text{graphene, } \epsilon_r \simeq 5) \\
 &\simeq 66 \sim 94 \sqrt{B[\text{T}]} [\text{K}] \quad (\text{bilayer graphene, } \epsilon_r \simeq 7 \sim 10) \\
 &\simeq 50 \sqrt{B[\text{T}]} [\text{K}] \quad (\text{GaAs, } \epsilon_r \simeq 13),
 \end{aligned} \tag{4.3}$$

which is smaller than the cyclotron energy ($\simeq 400 \sqrt{B[\text{T}]} [\text{K}]$ in zLL of graphene) but much larger than the Zeeman energy ($\frac{g\hbar eB}{2m_e} \simeq 1.3B[\text{T}] [\text{K}]$ in graphene) [18–21]. Therefore major

origin of the spin splitting at odd filling is not Zeeman splitting but electron correlation.

Generally, electron correlated systems have collective excitation whose energy is smaller than one-particle excitation, such as magnon in magnets and bosonic excitation in Luttinger liquid. Since spin-split quantum ferromagnet is isotropic, which has $SU(2)$ symmetry of the spins (because we can ignore Zeeman energy), a primary collective excitation is the skyrmion which costs half the energy of the simple single spin flip. This was experimentally observed in $\nu = 1$ state of GaAs quantum well using NMR [22].

4.3 Generalized quantum Hall ferromagnetism with multiple internal degrees of freedom of an electron

In addition to the spin degree of freedom, we consider another electron internal degrees of freedom (DOF), such as layers and valleys. Layer degrees of freedom exist in double layer quantum well systems and bilayer graphene (in bilayer graphene, layer DOF and valley DOF are equivalent in zLL as mentioned in Chapter 2).

4.3.1 Quantum Hall ferromagnetism with layers DOF

Here we first consider half filling of a LL in spinless quantum Hall systems with double-layer DOF. In the same way as that presented in the last subsection, pseudospin defined by the layer DOF align ferromagnetically between degenerated orbitals in the LL. The difference from the quantum Hall systems with spin DOF is that layer DOF does not have $SU(2)$ symmetry, while spins have $SU(2)$ symmetry. This is because interlayer Coulomb interaction is usually weaker than intralayer Coulomb interaction. Fig. 4.2 shows Bloch sphere of layer DOF. $SU(2)$ symmetry means that any point on the surface of Bloch sphere is energetically equivalent. However, $|u\rangle$ and $|b\rangle$ have larger energy than $|u\rangle + e^{i\phi}|b\rangle$ owing to larger intra-layer Coulomb repulsion than inter-layer Coulomb repulsion. Therefore the symmetry is reduced to be $U(1)$, which is the rotational symmetry along the equator of the Bloch sphere.

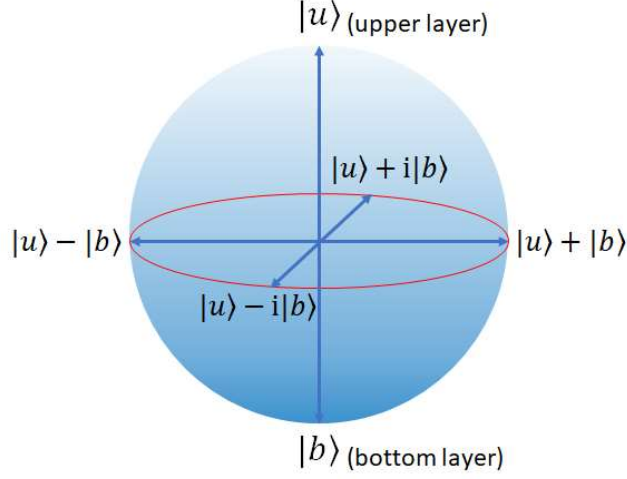


Figure 4.2: Bloch sphere of layer degree of freedom, whose basis $|u\rangle$ and $|b\rangle$ are defined by electron occupation of the upper layer and the bottom layer.

Instead of skyrmion excitation in SU(2) symmetric magnets, U(1) symmetry results in vortex excitation as a primary collective excitation, defined as the following spatial distribution of layer pseudospin \mathbf{m} [23] (Fig. 4.3):

$$\mathbf{m} = [\alpha\sqrt{1 - [m^z(r)]^2} \cos \phi, \sqrt{1 - [m^z(r)]^2} \sin \phi, m^z(r)], \quad (4.4)$$

or

$$|\mathbf{m}\rangle = \sqrt{\frac{1 + m^z(r)}{2}} |u\rangle + e^{i(\phi + \frac{\pi + \alpha}{2})} \sqrt{\frac{1 - m^z(r)}{2}} |b\rangle, \quad (4.5)$$

where, $\alpha = \pm 1$ refers to vortices and antivortices, $(x, y) = r(\cos \phi, \sin \phi)$ is the coordinate from the center of vortices (antivortices), and $m^z(r)$ is arbitrary function which satisfies the conditions $m^z(r = 0) = \pm 1$ and $m^z(r \rightarrow \infty) = 0$. $m^z(r = 0) = \pm 1$ refers to polarity of the pseudospin at the center of vortices (antivortices). Thus there are four flavors of vortices characterized by vorticity α and polarity $m^z(0)$.

When an electron moves around the vortex (antivortex) pseudospin texture, it feels spatially varying exchange field and adiabatically follows the local orientation of \mathbf{m} . This results in Berry phase ψ around vortices (antivortices) [23]

$$\psi = -\frac{1}{4} \int_{\Gamma} d^2\mathbf{r} \epsilon_{\mu\nu} \mathbf{m}(\mathbf{r}) \cdot [\partial_{\mu} \mathbf{m}(\mathbf{r}) \times \partial_{\nu} \mathbf{m}(\mathbf{r})] = m^z(0) \frac{\pi}{2}. \quad (4.6)$$

This extra Berry phase of $\pm \frac{\pi}{2}$ in real space is equivalent with the half of quantized magnetic flux. Since the number of magnetic flux quanta is equal to degeneracy of the LL in quantum Hall state, addition of one magnetic flux quantum corresponds to creation of one unoccupied state, or a hole. Therefore, creation of a vortex or antivortex corresponds to the creation of

$\pm e/2$ charge, depending on the sign of $m^z(0)$. This means that vortices and antivortices in a quantum Hall state are positively or negatively charged and contribute to charge transport.

In Eq. 4.4, rotation of pseudospin in xy-plane does not decay as a function of distance, and creation of one vortex causes rotation of pseudospins in the entire sample. Therefore, creation of a single vortex or antivortex is energetically forbidden at low temperature. Instead, vortex-antivortex pairs are excited in much smaller energy, because the vorticities of a vortex and an antivortex cancel each other and only have local impact on pseudospin fluctuation (Fig. 4.3). As long as vortices and antivortices are bound to be pairs, quasi-long-range order of the whole sample is preserved. Although the vorticity and the sign of charge are originally independent, bound vortex and antivortex favor to have opposite sign of charge to reduce the Coulomb energy. Therefore vortex-antivortex pairs are charge neutral and do not contribute to charge transport.

At higher temperature, creation of unbound vortices and antivortices is allowed, and they contribute to charge transport. Here, quasi-long-range order is broken. This phase transition is called Kosterlitz-Thouless transition.

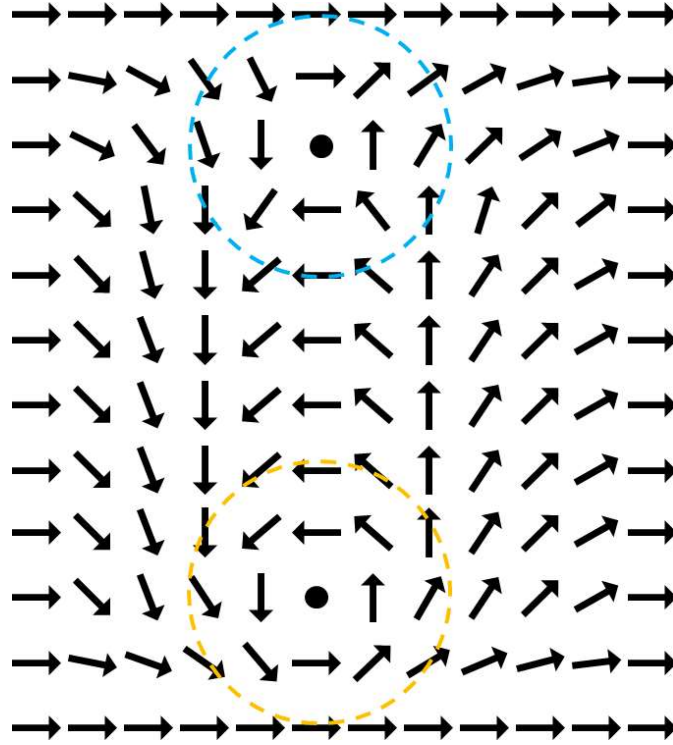


Figure 4.3: Schematic of a vortex (indicated by blue broken circle) and an antivortex (indicated by orange broken circle). When a vortex and an antivortex exist close to each other, the pair only affects locally the spin order, as the surrounding spins are aligned towards the right direction in this figure.

4.3.2 Quantum Hall ferromagnetism with spins and layers DOFs

Next, we consider half filled quantum Hall systems with 2×2 DOFs, such as spins and layers. Here, degeneracy of LLs are $4 \times BS/\Phi_0$ and half of them are occupied. Since we have two electrons for four-fold degenerated each orbital, configuration of spins and layers is represented by a two-particle state in $2 \times 2 = 4$ dimensional Hilbert space, instead of one-particle state in 2 dimensional Hilbert space (Bloch sphere) in previous cases. Considering the anti-symmetric restriction of two-Fermion state, two-particle state $|\Phi\rangle$ is written in the form of

$$|\Phi\rangle = |\chi_a \chi_b\rangle - |\chi_b \chi_a\rangle, \quad (4.7)$$

with the one-particle states χ_a and χ_b in $2 \times 2 = 4$ dimensional Hilbert space. Here we omit normalization constant.

Considering SU(2) symmetry of spin, rotational symmetry of the equator in Bloch sphere of the layer DOF, and symmetry between upper layer and bottom layer, we can restrict $|\Phi\rangle$ into these nonequivalent representations,

$$\begin{aligned} \chi_a &= |u\rangle \otimes |\mathbf{s}\rangle, \quad \chi_b = |b\rangle \otimes |\mathbf{s}\rangle \\ |\Phi\rangle &= (|ub\rangle - |bu\rangle) \otimes |\mathbf{s}\rangle, \end{aligned} \quad (4.8)$$

$$\begin{aligned} \chi_a &= |\mathbf{n}\rangle \otimes |\uparrow\rangle, \quad \chi_b = |\mathbf{n}\rangle \otimes |\downarrow\rangle \\ |\Phi\rangle &= |\mathbf{n}\rangle \otimes (|\uparrow\downarrow\rangle - |\downarrow\uparrow\rangle), \end{aligned} \quad (4.9)$$

$$\begin{aligned} \chi_a &= |u\rangle \otimes |\mathbf{s}\rangle, \quad \chi_b = |b\rangle \otimes |-\mathbf{s}\rangle \\ |\Phi\rangle &= |us\,b-\mathbf{s}\rangle - |b-\mathbf{s}\,us\rangle, \end{aligned} \quad (4.10)$$

where, $|\mathbf{s}\rangle$ and $|\mathbf{n}\rangle$ are arbitrary spin and layer states, respectively.

The first state (Eq. 4.8) is the cross product of layer singlet and arbitrary spin, which represents ferromagnetic (F) state. \mathbf{s} has SU(2) symmetry.

The second state (Eq. 4.9) is cross product of arbitrary layer and spin singlet. In case $|\mathbf{n}\rangle = |u\rangle$ or $|b\rangle$, the state is fully layer polarized (FLP), which has Z_2 symmetry. When $|\mathbf{n}\rangle = |u\rangle + e^{i\phi}|b\rangle$ (ϕ is an arbitrary angle from 0 to 2π), the state is layer coherent superposition (LC) which has U(1) symmetry. Intermediate of the LP and the LC state is partially layer polarized state (PLP), generally represented as $|\mathbf{n}\rangle = \sin\theta/2|u\rangle + e^{i\phi}\cos\theta/2|b\rangle$.

The third state (Eq. 4.10) cannot be written by a cross product. The upper layer and bottom layer have opposite spins, which represent layer antiferromagnetic (AF) state. In the representation of Eq. 4.10, it seems to have SU(2) symmetry of spin. However, considering Zeeman energy and Coulomb energy, \mathbf{s} tends to align in-plane with small tilting towards the magnetic field direction,

$$\begin{aligned} \chi_a &= |u\rangle \otimes |\rightarrow\rangle, \quad \chi_b = |b\rangle \otimes |\leftarrow\rangle, \\ |\Phi\rangle &= |u \rightarrow b \leftarrow\rangle - |b \leftarrow u \rightarrow\rangle, \end{aligned} \quad (4.11)$$

Here $|\rightarrow\rangle = \sin(\theta/2)|\uparrow\rangle + e^{i\phi}\cos(\theta/2)|\downarrow\rangle$ and $|\leftarrow\rangle = \sin(\theta/2)|\uparrow\rangle - e^{i\phi}\cos(\theta/2)|\downarrow\rangle$, with arbitrary angle $0 \leq \phi < 2\pi$ and $\cos\theta$ being proportional to the ratio of Zeeman energy to

Coulomb energy.

This state is called canted antiferromagnetic (CAF) state, and has $U(1)$ symmetry originated from ϕ .

The most stable state depends on parameters of the system.

4.4 $\nu = 0$ state of graphene

As derived in 1.2.3, zLL of bilayer graphene has 8-fold degeneracy per one orbital, originated from spins, layers, and $|0\rangle$ and $|1\rangle$ orbitals. According to the Hartree-fock theory [24], degeneracy of spins and layers are rifted first, and degeneracy of $|0\rangle$ and $|1\rangle$ orbitals is lifted only at odd filling such as $\nu = \pm 1$ and ± 3 . Here we consider half filling of zLL $\nu = 0$, where the degeneracy of orbitals is not rifted and we only have to consider spin and layer DOF. Therefore, the problem is reduced to the one discussed in the previous section, and the possible choices of spin and layer occupation are ferromagnetic (Eq. 4.8), layer polarized (Eq. 4.9), and antiferromagnet (Eq. 4.11). Which state becomes most stable depends on parameters such as the ratio between Coulomb interaction, Zeeman energy, and layer polarization energy. Calculation for bilayer graphene gives a phase diagram shown in Fig. 4.4 [25].

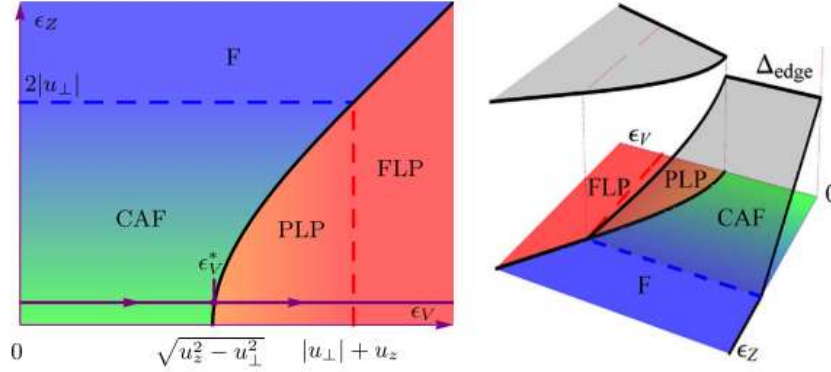


Figure 4.4: Phase diagram of the $\nu=0$ state of bilayer graphene obtained from theoretical calculation [25]. Left figure is bulk phase diagram as a function of Zeeman energy ϵ_Z and layer polarization energy ϵ_V . Right figure shows the energy gap of the edge state. Only the F state has a zero-gap edge mode.

Here, horizontal axis is the layer polarization energy ϵ_V tuned by application of out-of-plane electric field (displacement field D) and vertical axis is Zeeman energy ϵ_Z determined by the total magnetic field. u_z and u_\perp are the inter-layer and intra-layer exchange energies, which are fixed in this phase diagram. The origin corresponds to $D = 0$ and $B_{\text{total}} = B_\perp$. Close to the origin, the CAF state (Eq. 4.11) is stabilized. Canted angle is determined by the ratio of Zeeman energy to the intra-layer exchange energy, $\theta = \epsilon_Z/2u_\perp$. Under an application of a displacement field, phase transition occurs and LP (Eq. 4.9) state is stabilized. In the LP state region, crossover from the PLP state to the FLP state occur. When Zeeman energy

is increased, canted angle $\theta = \epsilon_Z/2u_\perp$ increases and the CAF state is continuously changed to the F state.

Phase changes from CAF to F, and PLP to FLP are continuous crossover, where the order parameter is gradually changed. On the other hand, phase transition between the CAF and the PLP state is thought to be first order transition, according to the mean-field theory [25–27].

To discuss further distinction between these insulating states, we consider Hall conductivity and edge channels. The F state has spin splitting at zero energy, therefore has spin dependent Hall conductivity $\sigma_\uparrow = +2e^2/h$, $\sigma_\downarrow = -2e^2/h$. This results in a spin-helical edge channel. The LP state has layer polarization, which is equivalent to valley polarization, and therefore has valley dependent Hall conductivity $\sigma_{K(u)} = +2e^2/h$, $\sigma_{K'(b)} = -2e^2/h$. However, LP state does not have an edge channel unless the sample edge is zigzag, because of the valley scattering at the sample edge. The CAF state has spin dependent layer polarization, where \rightarrow spins are polarized in the upper layer and \leftarrow spins are polarized in the bottom layer (Eq. 4.11). This is as if effective displacement field is applied in opposite directions for opposite spins. Therefore, the Hall conductivity is both spin and layer (valley) dependent, $\sigma_{\rightarrow K(u)} = +e^2/h$, $\sigma_{\rightarrow K'(b)} = -e^2/h$, $\sigma_{\leftarrow K(u)} = -e^2/h$, and $\sigma_{\leftarrow K'(b)} = +e^2/h$. This discussion is mathematically expressed by following mean-field Hamiltonian for the CAF state,

$$\begin{aligned} H_{\text{MF}} &= \sum_p c_p^\dagger h c_p \\ h &= \epsilon_Z I \otimes s_z + \Delta_{\text{CAF}} \tau_z \otimes [\sin(\phi) s_x + \cos(\phi) s_y]. \end{aligned} \quad (4.12)$$

Here, p is the index of BS/Φ_0 -fold degenerated orbitals in the zLL, and $c_p = (c_{p,K,\uparrow}, c_{p,K',\uparrow}, c_{p,K,\downarrow}, c_{p,K',\downarrow})$ is four-component vector of creation operators in the valley \otimes spin space. Δ_{CAF} is the energy gap of the CAF state, whose energy scale is comparable to $e^2/4\pi\epsilon l_B$. The first term is Zeeman energy and second term is the mass term, which produces energy difference between the two valleys. The sign of mass term is determined by the expectation value of $\sin\phi s_x + \cos\phi s_y$. Therefore, opposite spins $|\rightarrow\rangle$ and $|\leftarrow\rangle$ ($\langle\rightarrow|\sin\phi s_x + \cos\phi s_y|\rightarrow\rangle = 1$ and $\langle\leftarrow|\sin\phi s_x + \cos\phi s_y|\leftarrow\rangle = -1$) have opposite sign of the valley Hall conductivities, as illustrated in Fig. 4.5. Similarly to the LP state, edge channel is absent in the CAF state due to valley scattering at the sample edge.

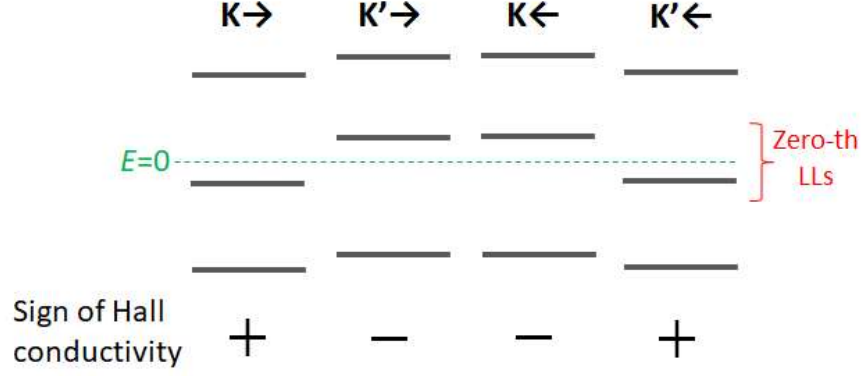


Figure 4.5: Schematic of LLs for $\epsilon_Z \ll \Delta_{\text{CAF}}$ in Eq.4.12.

Experimentally, conductance plateau at $\nu = 0$ has been reported in many papers [28–32]. After the method of encapsulating graphene with h-BN is established, highly uniform devices are realized and several experiments in dual-gated devices revealed that the CAF state and the LP state are observed as separated insulating regions around zero carrier density in a plane defined by the displacement field and the carrier density [33, 34] (Fig. 4.6).

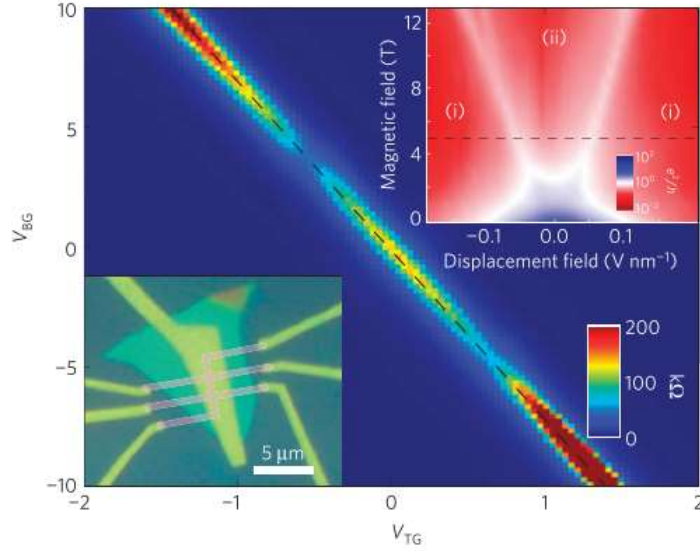


Figure 4.6: Dual gate dependence of four terminal resistance of bilayer graphene under a magnetic field of 5 T [33]. The inset in left bottom is optical microscope image of bilayer graphene sample encapsulated by h-BN. The inset in right upper is resistance as a function of displacement field and magnetic field, with fixed carrier density zero.

Crossover between the CAF and F states was also observed as a change of two-terminal resistance, which indicates appearance of the edge channel in F state [33] (Fig. 4.7).

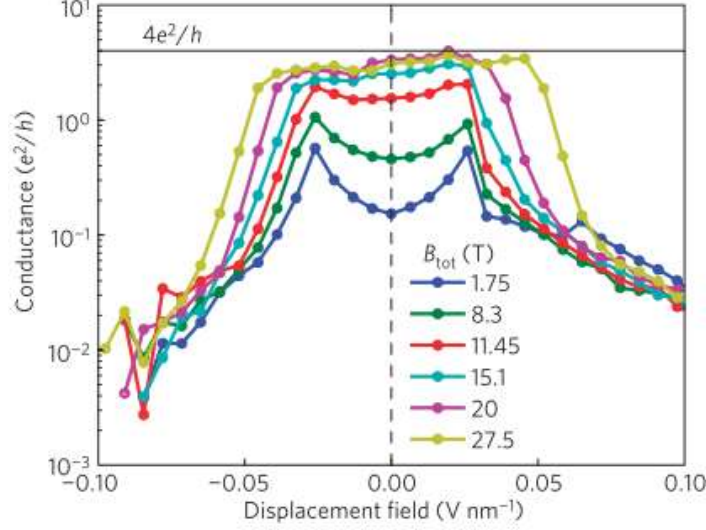


Figure 4.7: Displacement field dependence of two terminal conductance in bilayer graphene [33]. Perpendicular magnetic field is fixed at $B_{\perp} = 1.75$ T and in-plane magnetic field B_{\parallel} is changed. Different colors indicate different total magnetic field $B_{\text{tot}} = \sqrt{B_{\perp}^2 + B_{\parallel}^2}$. As B_{tot} increase, Zeeman energy increase and crossover from the CAF to the F state occur, which lead to existence of spin helical edge channel.

These experimental observations are well accounted for by the theory we have introduced, however, recently, an intermediate phase between the CAF and PLP, which is not yet explained by theory was observed [35] (Fig. 4.8). We can see double peak in resistance between the CAF and the LP state, indicating the intermediate state between them.

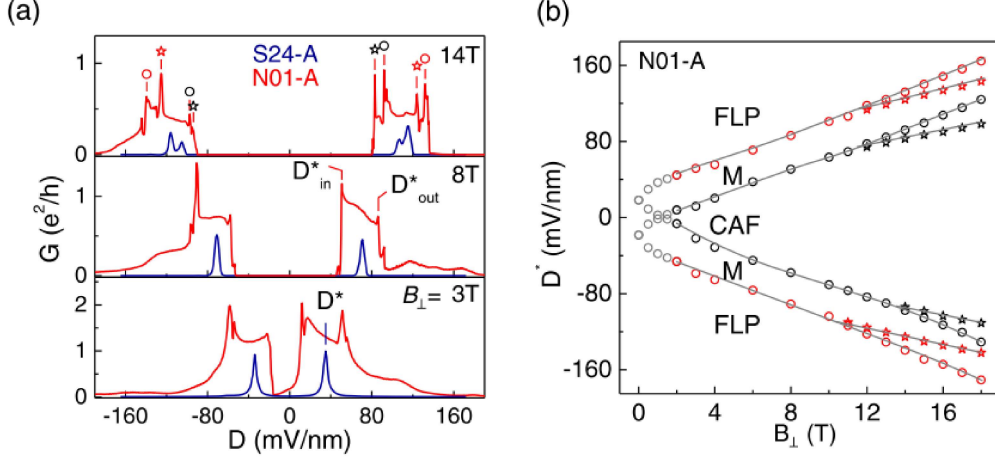


Figure 4.8: (a) Displacement field dependence of two terminal conductance of bilayer graphene encapsulated by h-BN under perpendicular magnetic fields of 3, 8, and 14 T. Blue and red curve denote different samples S24-A and N01-A, respectively. N01-A have thicker h-BN (50 nm) than S24-A (40 nm). In N01-A, conductance peak at the border of the CAF and the LP state D^* split into two peaks D_{in}^* and D_{out}^* ($B = 3$ and 8 T). At $B = 14\text{ T}$, D_{in}^* and D_{out}^* peaks further split into two peaks as indicated by \star and \circ . (b) Position of peaks in D and B phase diagram. The region between two peaks D_{in}^* (black circle) and D_{out}^* (red circle) is the intermediate state denoted as M.

Most of the previous experiments have been done in constant low temperature around $1\sim 2\text{ K}$, and the temperature dependent phase transition has not yet been understood, even though fertile phase transitions are expected in the $\nu = 0$ state of bilayer graphene. For example, quantum phase transition between the CAF and the LP state is expected to be first order transition according to mean-field theory, but its hysteretic behavior has not been explored yet. In the CAF state, Kosterlitz Thouless transition is expected due to its $U(1)$ symmetry, which is also experimentally elusive.

All the experiments above are resistance measurement in dual gated samples, and we cannot obtain direct evidence of ferromagnetism or antiferromagnetism from them. One way to extract the spin information is spin current transport measurement. Although it is not realized in bilayer graphene, spin current transport in the CAF state of monolayer graphene was reported [36, 37]. They injected spin current into the CAF state using spin polarized edge state of $\nu = -1$ quantum Hall ferromagnetic state, and observed a long-distance spin transport, which indicates presence of a spin order. In easy-plane magnets such as the CAF state, coherent rotation of spins is thought to mediate a superfluid-like spin current [38–42]. The observation of long-distance spin transport is one signature of the spin superfluidity, but cannot be an evidence. The evidence will be obtained by critical behaviors around the critical temperature or critical current, although it is still difficult due to the limitation of spin injection temperature and magnitude of spin current.

Another ways to directly measure the spin order is optical methods such as infrared spectroscopy and Raman spectroscopy, and NMR which was often used to measure quantum Hall magnetism of GaAs quantum well systems. The former has not yet been done, however, it should provide useful information about the nature of quantum Hall magnetism in graphene. The later is more difficult, because graphene has less nuclear spin than GaAs. For that, C^{13} isotope-enriched graphene might be useful.

Chapter 5

Charge neutral current generation in quantum Hall antiferromagnet of bilayer graphene

5.1 Motivation

Two kinds of charge neutral currents, spin current and valley current are introduced in chapter 3. Spin current is the most promising charge neutral current which can be directly coupled with magnetic memory. Graphene is suitable material as a spin transport channel but conversion between the electrical current and spin current in pristine graphene is difficult due to its small spin-orbit interaction. Although adatom decoration and substrate effects enable extrinsic spin Hall effect in graphene, such decorations decrease the mobility and homogeneity of graphene, and should disturb the valley Hall effect and other fascinating electronic properties of graphene.

Valley current is a flow of electrons into opposite directions between those belonging to different valley of the band structure, and specific to two-dimensional honeycomb lattice systems. Compared with the spin Hall angle whose maximum value ever reported is around 50 [43], valley Hall angle can be giant by applying out-of-plane electric field in bilayer graphene. In previous research of valley Hall effect in bilayer graphene [16], valley Hall angle is estimated to reach 1000, where the electrical conductivity is of the order of 10^{-7} S (10 M Ω) and valley Hall conductivity is around 10^{-4} S ($4e^2/h$). This means that valley current can be generated more efficiently than spin current from the charge current.

To make use of both advantages of spin current and valley current, we have to couple spin and valley.

Since valley angular momentum is a kind of orbital angular momentum, naively thinking, we must have SOI to couple them. Without SOI, opposite valleys are symmetric for each spin and there is no reason to have one-to-one correspondence between each spin and valley (Fig. 5.1). However, SOI is not the only way to break the valley symmetry for each spin. Even if Hamiltonian does not have a symmetry breaking term, the symmetry of state can be broken spontaneously in a correlated system. This is the case of the canted antiferromagnetic (CAF) state in graphene, where the valley symmetry is broken spontaneously in association with emergence of the antiferromagnetic order in a highly correlated quantum Hall system.

Therefore, it should be possible to couple spin and valley using this CAF state.

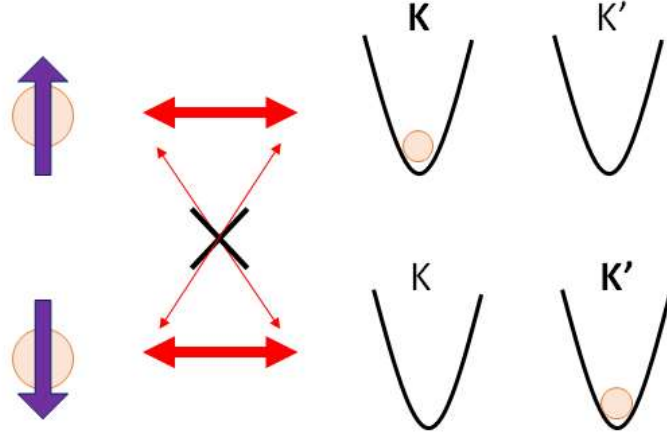


Figure 5.1: Schematic of the concept of one-to-one correspondence between spins and valleys.

5.2 Proposal of spin-valley Hall effect

Canted layer antiferromagnetic state has opposite in-plane spin between the upper and bottom layers. This state is expressed by mean-field Hamiltonian in Eq. 4.12 [25–27], and has the spin-dependent mass term (Fig. 4.5).

This results in spin and valley contrasting Hall conductivity and leads to generation of spin-valley Hall current perpendicular to in-plane electric field (or current) (Fig. 5.2). Here, spin-valley current is defined by $J_{SV} = J_{K\leftarrow} - J_{K'\leftarrow} - J_{K\rightarrow} + J_{K'\rightarrow}$.

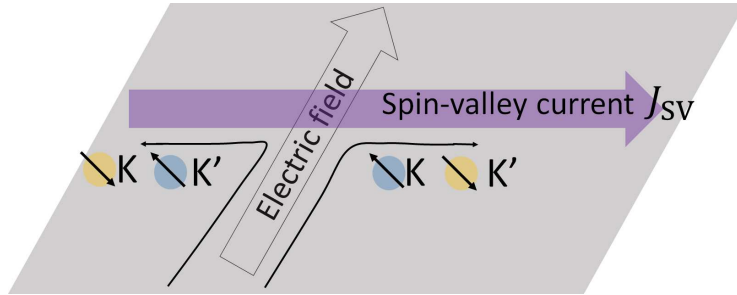


Figure 5.2: Schematic description of the spin-valley Hall effect and definition of the spin-valley current. Blue (yellow) circles indicate electrons in the top (bottom) layer, and arrows indicate spin.

The spin-valley current is a kind of charge neutral current, however, its existence seems to have been overlooked because it carries neither spin nor valley degrees of freedom.

The spin-valley Hall effect is phenomenologically similar to spin Hall effect and valley Hall effect, however, it is very different from previous charge neutral current generation in

terms of symmetry and electron correlation. Generally, to realize non-zero flavor contrasting Hall conductivity, either the SOI or the breaking of spatial inversion symmetry is necessary. As described in Chapter 3, pristine monolayer graphene and bilayer graphene have neither of them. Therefore previous researches introduced SOI using adatoms and substrate [11–14], or introduced spatial inversion symmetry breaking using substrates [15] or applying out-of-plane electric field for bilayer graphene [16, 17].

In the CAF state, spatial inversion symmetry is broken spontaneously by electron correlation. Previously, the role of electron correlation effect in charge neutral current generation has not been well understood. Because electron correlation is sensitive to the filling factor and out-of-plane electric field, charge neutral current generation in the CAF state is gate tunable.

In addition, the spin-valley Hall effect allows for the coupling between spin and valley degrees of freedom without SOI. Because the Hall conductivity is spin and valley contrasting, if we inject an opposite current for each spin, or a spin current, a valley current is expected to flow in the transverse direction (Fig. 5.3). This mutual conversion between spin current and valley current may open up a new possibility of electrical generation and detection of a spin current in graphene with high efficiency.

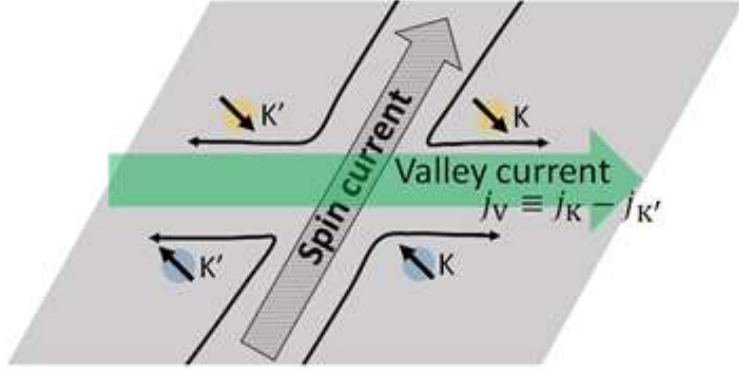


Figure 5.3: Schematic description of the spin current to valley current conversion. The spin current (opposite charge current between the layers) generates the valley current in its transverse direction.

5.3 Nonlocal transport measurement

Similarly to previous researches of spin Hall effect and valley Hall effect, we perform nonlocal transport measurement to experimentally demonstrate the spin-valley Hall effect. Here we describe the semiclassical model for charge neutral current generation and detection.

In Fig. 5.4, when in-plane electric field E is applied between the left two terminals, electrical current $I \propto E\sigma_{xx}$ flows there. Here, due to spin-valley Hall conductivity σ_{SVH} , spin-valley current $J_{SV,in} \propto E\sigma_{SVH}$ is also generated. The spin-valley current decays during the propagation in the longitudinal direction of the Hall bar. The decay is written as $J_{SV,out} = J_{SV,in} \exp(-L/l)$, where, l is the scattering length, L is the Hall bar length, and $J_{SV,out}$ is the decayed spin-valley current in the right side of the Hall bar. Then the

spin-valley current generates a nonlocal voltage V between the right two terminals. Here, $V \propto \rho_{\text{SVH}} J_{\text{SV,out}} = \frac{\sigma_{\text{SVH}}}{\sigma_{\text{SVH}}^2 + \sigma_{xx}^2} J_{\text{SV,out}}$. By all these relationships being combined, we obtain the nonlocal resistance as

$$R_{\text{NL}} = V/I \propto \frac{\sigma_{\text{SVH}}}{\sigma_{xx}(\sigma_{\text{SVH}}^2 + \sigma_{xx}^2)} \exp(-L/l) . \quad (5.1)$$

Including the proportional constant determined by the Hall bar dimensions and scattering length, it becomes [16, 17]

$$R_{\text{NL}} = \frac{W}{2l} \frac{\sigma_{\text{SVH}}}{\sigma_{xx}(\sigma_{\text{SVH}}^2 + \sigma_{xx}^2)} \exp(-L/l) , \quad (5.2)$$

where, W is width of the Hall bar.

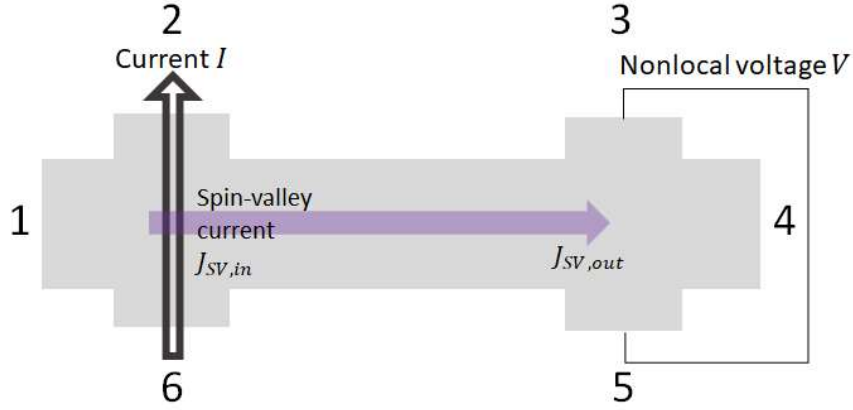


Figure 5.4: Schematic description of the nonlocal transport experiment. A charge current is injected between the terminals 2 and 6, and the nonlocal transport mediated by the spin-valley current is measured as the voltage induced between the terminals 3 and 5.

Since the Hall conductivity arise from intrinsic mechanism, σ_{SVH} should be constant $4e^2/h$. In this case, Eq.5.1 and 5.2 lead to following scaling dependences between R_{NL} and ρ ,

$$\begin{aligned} R_{\text{NL}} &\propto \rho_{xx}^3 \quad (\sigma_{xx} \gg \sigma_{\text{SVH}}) \\ &\propto \rho_{xx} \quad (\sigma_{xx} \ll \sigma_{\text{SVH}}) . \end{aligned} \quad (5.3)$$

Since the first and second components of Eq. 5.2, $W/2l$ and $\sigma_{\text{SVH}}/(\sigma_{xx}(\sigma_{\text{SVH}}^2 + \sigma_{xx}^2))$ can be order of unity, the ratio between R_{NL} and ρ can be around 1/10, assuming the same order of L and l . This value is much larger than the nonlocal resistance originated from trivial Ohmic current diffusion.

Ohmic current diffusion effect on nonlocal resistance can be estimated by the theory of van der Pauw. Here we assume any shape of a two-dimensional conductor with homogeneous resistivity ρ (Fig. 5.7). When it has four electrodes, four-terminal resistances and the resistivity ρ have following relationship

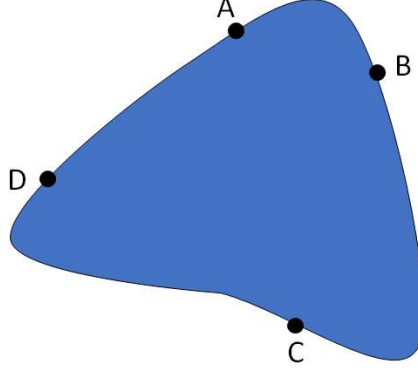


Figure 5.5: Four terminal measurement of any shape of 2D conductor.

$$\exp(-\pi R_{DC,AB}/\rho) + \exp(-\pi R_{AD,BC}/\rho) = 1, \quad (5.4)$$

where, $R_{ab,cd} = V_{a-b}/I_{c-d}$.

Applying this general formula into Hall bar, we obtain

$$\exp(-\pi R_{35,26}/\rho) + \exp(-\pi R_{23,56}/\rho) = 1. \quad (5.5)$$

Since $R_{35,26} = R_{NL}$, $R_{23,56} \simeq R_{23,14} = R_L$, and $\rho \simeq (W/L)R_L$, we can rewrite Eq. 5.5 as following,

$$\begin{aligned} \exp(-\pi L R_{NL}/W R_L) + \exp(-\pi L/W) &= 1 \\ R_{NL} &= -\frac{W R_L}{\pi L} \ln[1 - \exp(-\pi L/W)] \end{aligned} \quad (5.6)$$

In case of our Hall bar sample whose dimension is $L=2.5 \mu\text{m}$ and $W=1.0 \mu\text{m}$,

$$R_{NL} \simeq R_L \times 5 \times 10^{-5} \quad (5.7)$$

5.4 Sample fabrication

Since the scattering length of spin-valley current is expected to be at the same order with that of spin current and valley current, which are a few microns, we fabricated Hall bar samples with the size of a few microns (Fig.5.6). Hall bar samples are encapsulated by h-BN and sandwiched by metal top gate and graphite back gate (Hall bar 1) or Si substrate back gate

(Hall bar 2).

In the fabrication process, we first prepared bilayer graphene and h-BN on $\text{SiO}_2(285\text{nm})/\text{Si}$ substrate by mechanical exfoliation technique. The number of layers in each graphene flake was identified by contrast of optical microscope image. After choosing clean bilayer graphene and h-BN using AFM, a h-BN flake (30 nm thickness) was picked up by a stamp made by polycarbonate thin film on round-shaped PDMS (Fig. 5.7). Then we picked up bilayer graphene by the h-BN flake, and release them on another h-BN flake (Fig. 5.7). For Hall bar 1, the h-BN/graphene/h-BN stack was again picked up and released on 9-nm thick graphite. After making (graphite/h-BN/bilayer graphene/h-BN) stack, we annealed them at 380°C in an Ar/H_2 atmosphere for 1.5 hours to remove polycarbonate residue.

Then top gate (Pd 5 nm/ Au 35 nm) and Ohmic contacts (Ti 2 nm/ Pd 20 nm/ Au 100 nm) were defined by electron beam lithography and metal deposition by electron beam evaporators. The stack was etched into a Hall bar by means of reactive ion etching in an $\text{Ar}/\text{CF}_4/\text{O}_2$ atmosphere.

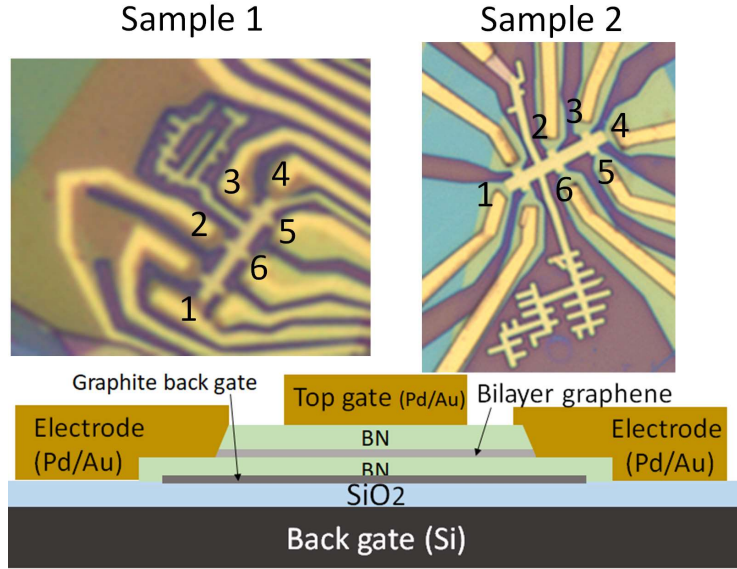


Figure 5.6: Optical microscope images of the two devices used for the experiments (upper panels). The two Hall bars have the width of $1\ \mu\text{m}$ and length between 2 and 3 (6 and 5) terminals of $2.5\ \mu\text{m}$. One side of the Hall bar 1 has a jagged region sticking out of the Hall bar between the terminals 2 and 3 to examine the contribution of edge transport to the nonlocal resistance. The lower panel shows the schematic cross section of the device. The bilayer graphene is encapsulated by hexagonal boron nitride with thickness of $35\sim 45\ \text{nm}$, and sandwiched between the top gate and graphite back gate. Hall bar 2 does not have graphite back gate and p-doped Si substrate is used as a back gate.

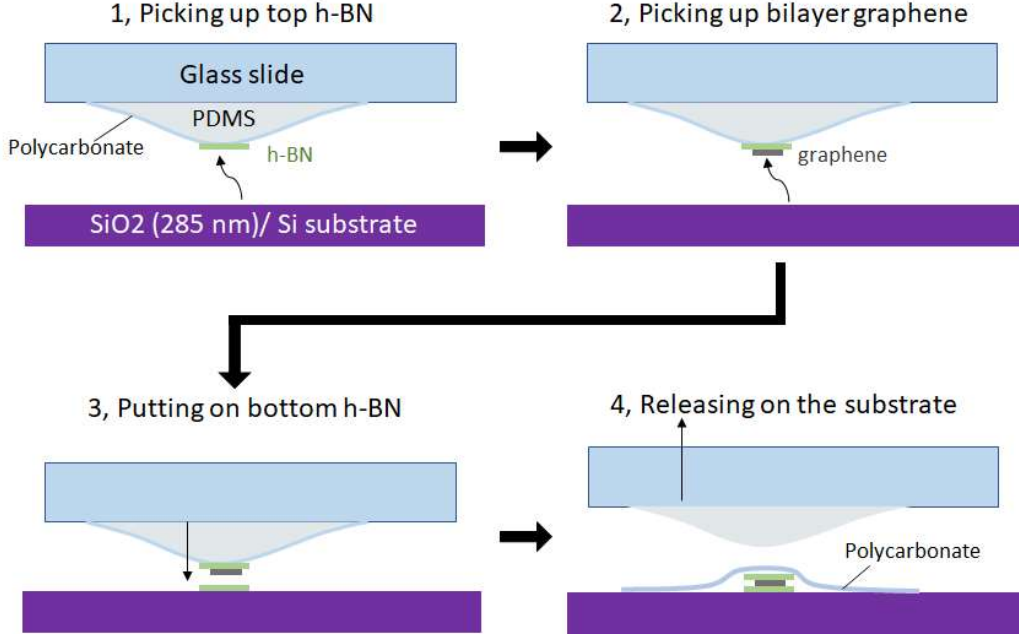


Figure 5.7: Fabrication processes of h-BN/ bilayer graphene/ h-BN stack.

5.5 Dual gate dependence

By tuning top gate and back gate voltages V_{TG} and V_{BG} , we can tune carrier density n and out-of-plane electric field (displacement field D) based on the relationships

$$n = \frac{\epsilon_{BN}\epsilon_0}{ed_{BN}}(V_{TG} - V_{TG}^0) + \frac{\epsilon_{SiO_2}\epsilon_0}{ed_{SiO_2+BN}}(V_{BG} - V_{BG}^0) \quad (5.8)$$

$$D = -\frac{\epsilon_{BN}}{d_{BN}}(V_{TG} - V_{TG}^0) + \frac{\epsilon_{SiO_2}}{d_{SiO_2+BN}}(V_{BG} - V_{BG}^0). \quad (5.9)$$

Here, $\epsilon_{BN} = 3.7$ and $\epsilon_{SiO_2} = 3.9$ are the relative dielectric constants of h-BN and SiO_2 , d_{BN} and d_{BN+SiO_2} are thicknesses of h-BN and SiO_2 measured by AFM. V_{TG}^0 (V_{BG}^0) is the offset of the top (back) gate voltage due to environmental doping.

In Fig. 5.8, n and D dependence (obtained by linear conversion from dual gate dependence using Eq. 5.8) of local resistance $R_L = V_{2-3}/I_{1-4}$ and nonlocal resistance $R_{NL} = V_{3-5}/I_{2-6}$ measured at temperature $T = 1.7K$ with Hall bar 2 are shown. Injected current is less than 5 nA which is in the linear transport regime.

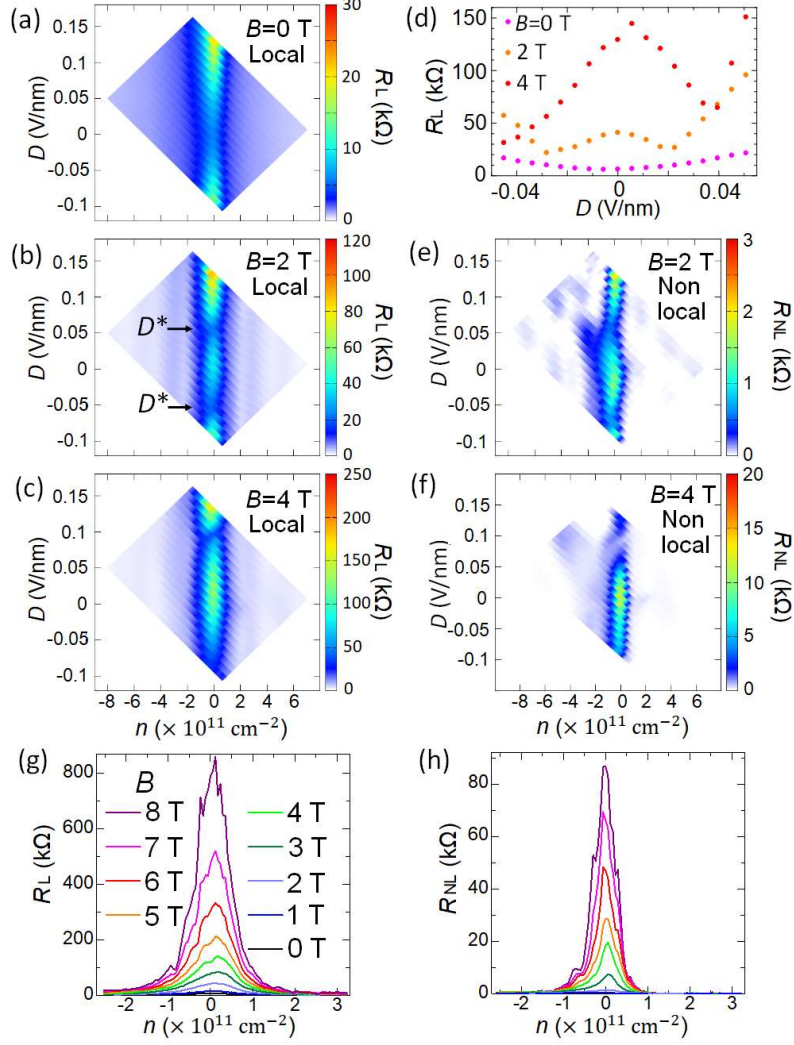


Figure 5.8: Carrier density n and displacement field D dependence of the local resistance R_L and nonlocal resistance R_{NL} measured at $T=1.7$ K for Hall bar 2. (a), (b), (c) n and D dependence of R_L measured at the magnetic field B of 0 T (a), 2 T (b), and 4 T (c), respectively. n and D are calculated from the top gate and back gate voltages using the literature value of dielectric constants of h-BN and SiO $_2$ and measured thickness of h-BN (Eq. 5.8). (d) R_L along the $n = 0$ lines in (a), (b), and (c), showing D dependence for the magnetic fields B of 0, 2, and 4 T. (e), (f) n and D dependence of R_{NL} for $B = 2$ T (e), and 4 T (f), respectively. (g), (h) n dependence of R_L (g) and R_{NL} (h) along the $D = 0$ line, measured at the magnetic field of 0 to 8 T.

First we focus on R_L . At zero magnetic field, R_L at $n = 0$ monotonically increases with the displacement field D due to the opening of the single particle band gap (Fig. 5.8(a)).

When the magnetic field of 2 T is applied, a local maximum appears around the $D = n = 0$ indicating development of the CAF insulating state (Fig. 5.8(b)), similarly to the previous reports introduced in Chapter 4 [33, 34]. This state becomes more robust with increasing magnetic field due to the reduced kinetic energy (Fig. 5.8(c)). When the displacement field is increased from zero, R_L at $n = 0$ once decreases and again increases (Fig. 5.8(d)). This upturn is attributed to closing of the CAF gap and phase transition to another insulating state, layer polarized (LP) state as reported in previous studies [33, 34].

From the value of D at the boundary between CAF and LP states (D^* in Fig. 5.8), we can estimate the energy gap of the CAF state at $D = 0$. This estimation is based on the one-particle model based on the mean-field Hamiltonian (Eq. 4.12). At $D = 0$, spin contrasting mass term split the zLLs as shown in the left figure of Fig. 5.9. As increasing D , valley dependent energy difference $\Delta(D)$ is introduced. At $D = D^*$, $\Delta(D^*)$ becomes equal to Δ_{CAF} and the energy gap close (the middle figure of Fig. 5.9). The function $\Delta(D)$ under zero magnetic field is known to be [44]

$$\Delta(D) = 130 \times D \text{ (V/nm)} \text{ (meV)}. \quad (5.10)$$

Assuming that $\Delta(D)$ under magnetic field is the same with that without magnetic field, or ignoring correlation energy of the LP state, we obtain the CAF energy gap

$$\Delta_{\text{CAF}} = 130 \times D^* \text{ (V/nm)} \text{ (meV)} \simeq 40 \text{ K/T}. \quad (5.11)$$

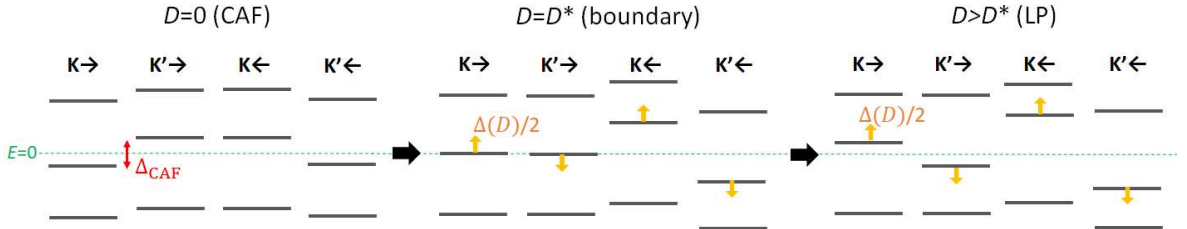


Figure 5.9: Energy diagram of LLs in different values of D .

We then discuss nonlocal resistance R_{NL} for the CAF state in Figs 5.8(e), (f), and (h). Similarly to R_L , R_{NL} becomes maximal at $D = n = 0$. The peak value of R_{NL} is more than $1/50$ of R_L . Such a large nonlocal resistance cannot appear in trivial Ohmic current diffusion as derived in Eqs. 5.6 and 5.7, indicating the nontrivial effect such as charge neutral current generation. R_{NL} is suppressed at the phase boundary between the CAF and the LP states, and has the same order of magnitudes in these two insulating states.

Figs. 5.8(g) and (h) show the carrier density dependence of R_L and R_{NL} at $D = 0$ under the magnetic field of 0 to 8 T. The peak of R_{NL} is sharper than that of R_L implying a nonlinear relationship between R_{NL} and R_L as discussed in the following section. Similar n and D dependences were observed in Hall bar 1 (Fig. 5.10).

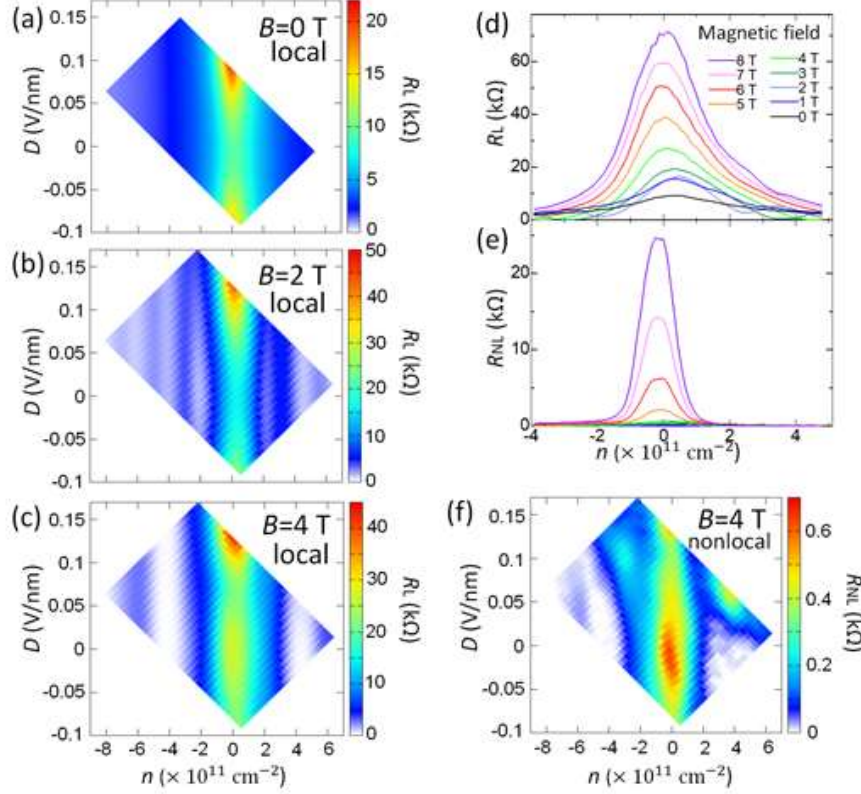


Figure 5.10: Carrier density n and displacement field D dependence of the local resistance R_L and nonlocal resistance R_{NL} measured at $T=1.7 \text{ K}$ for Hall bar 1. (a), (b), (c) n and D dependence of R_L measured at the magnetic field B of 0 T (a), 2 T (b), and 4 T (c), respectively. (d, e) n dependence of R_L (d) and R_{NL} (e) along the $D = 0$ line of a-c and f, respectively, measured for the magnetic field of 1 to 8 T. (f) n and D dependence of R_{NL} measured at the magnetic field B of 4 T.

5.6 Scaling relationship

To confirm that the origin of measured R_{NL} is the charge neutral current, we check the relationship expected from semiclassical model described in Eqs. 5.2 and 5.3. We measure R_L and R_{NL} for $D = 0$ while sweeping the temperature from 1.7 to 32 K with the magnetic field as a parameter. The temperature in this range is less than the energy gap of the CAF state estimated from the boundary displacement field between the CAF state and the LP state, which is proportional to the magnetic field: $\Delta_{\text{CAF}}/B \simeq 40 \text{ K/T}$ (Eq.5.11).

We then plot the peak values of R_{NL} vs R_L (at $n \simeq 0$, see Figs. 5.8(g) and (h)) in Fig. 5.11. We find that all data points obtained with Hall bar 1 fall on a single curve of the cubic scaling for $20 \text{ k}\Omega < R_L < 80 \text{ k}\Omega$. In Hall bar 2, we observe linear scaling for R_L exceeding

90 k Ω . Below $R_L \simeq 90$ k Ω , the scaling exponent becomes larger and becomes cubic below $R_L \simeq 30$ k Ω .

The cubic scaling relationship holds also for a small but non-zero carrier density (Fig. 5.12) and accounts for the sharper peaks of R_{NL} than R_L shown in Figs. 5.8(g), (h) and Figs. 5.10(d), (e).

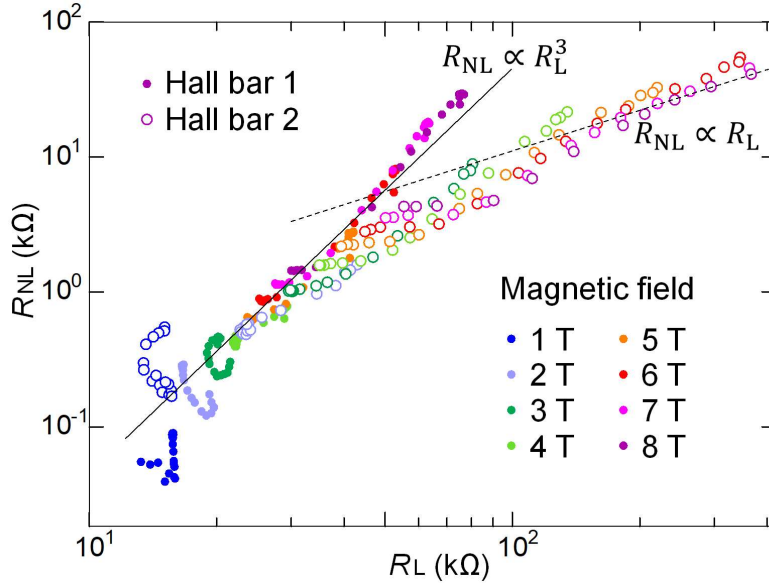


Figure 5.11: Scaling relationship between R_L and R_{NL} . Peak values of R_{NL} along the $D = 0$ line are plotted as a function of that of R_L obtained in the range of temperature of 1.7 to 32 K and magnetic field of 1 to 8 T. The data points of the same color are taken at the same magnetic field. Dots and open circles denote the data from Hall bar 1 and Hall bar 2, respectively. The solid (broken) line corresponds to the cubic (linear) scaling.

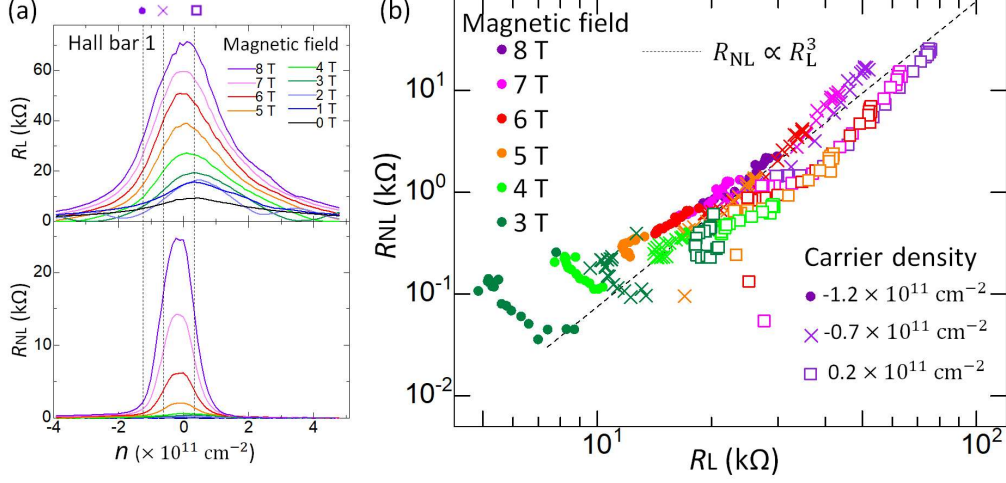


Figure 5.12: Scaling relationship between R_L and R_{NL} at finite carrier densities. (a) Carrier density n dependence of R_L and R_{NL} along the $D = 0$ line in Hall bar 1, measured at the magnetic field of 0 to 8 T. The carrier densities at the purple dot, cross, and open square are $-1.2 \times 10^{11} \text{ cm}^{-2}$, $-0.7 \times 10^{11} \text{ cm}^{-2}$, and $0.2 \times 10^{11} \text{ cm}^{-2}$, respectively. (b) Peak values of R_{NL} along the $D = 0$ line plotted as a function of that of R_L obtained in the range of temperature of 1.7 to 32 K and magnetic field of 1 to 8 T. The data points of the same color are taken at the same magnetic field. Dots, crosses, and open squares denote the data at three different carrier densities in (a), respectively. The broken line corresponds to the cubic scaling.

As we discussed before, semiclassical model of the intrinsic spin-valley Hall effect gives us the cubic and linear scaling dependence between R_L and R_{NL} (Eq. 5.3) and accounts for the experimental results. Obtained scaling relationship is the evidence of nonlocal transport mediated by a charge neutral current generated by the intrinsic Hall effect.

The absolute value is also consistent with Eq. 5.2. In Fig. 5.13, we show the measured R_{NL} vs R_L , that in previous experiment of valley Hall effect in bilayer graphene [16], and that calculated from Eq. 5.2.

R_{NL} in our measurement at the CAF state is comparable with R_{NL} in the valley Hall effect experiment and semiclassical model. However, we observe cubic scaling up to $\rho \simeq 30 \text{ k}\Omega$ although semiclassical model exhibits scaling crossover around $\rho = h/4e^2$. Also in valley Hall effect, cubic scaling up to much higher $\rho (\simeq 2 \text{ M}\Omega)$ has been observed [16]. Although the reason of this contradiction is not clear yet, one possibility is that the charge conductivity σ_{xx} in Eq. 5.2 may not simply be measured by the electrical current divided by the in-plane electric field, but be defined as effective conductivity for the thermally activated carriers [17]. Another possibility is that the spin-valley Hall (valley Hall) conductivity is reduced because of the sample dependent inhomogeneity.

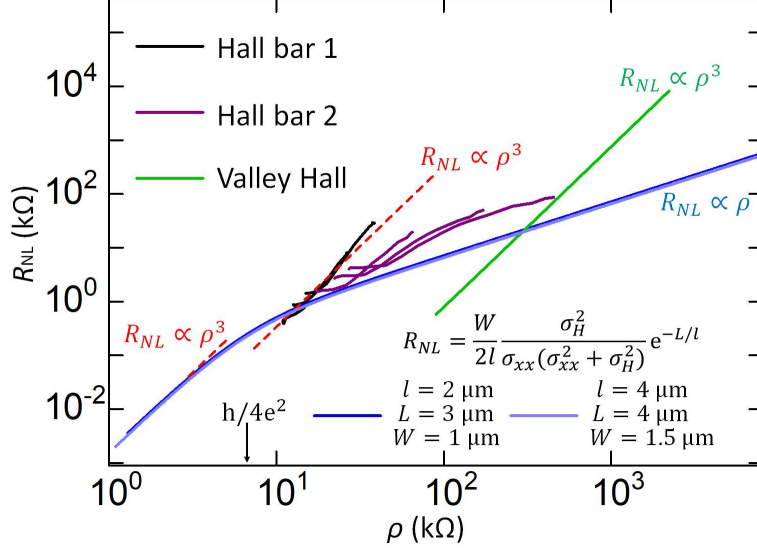


Figure 5.13: Comparison of R_{NL} in the CAF state, valley Hall state, and semiclassical model. Black and purple solid lines indicate R_{NL} at $D = n = 0$ obtained in the range of temperature of 1.7 to 32 K and magnetic field of 4, 6, 8 T measured in Hall bar 1 and Hall bar 2, respectively. Green solid line is R_{NL} under zero magnetic field and finite displacement field in bilayer graphene, obtained from cubic fitting lines Fig. 3c of ref. [16]. Blue and light-blue lines indicate Eq. 5.2 for different parameters of device dimensions W (Hall bar width) and L (Hall bar length), which correspond to our devices and device in ref. [16], respectively. l (scattering length of charge neutral current) are determined to realize best fit of the experimental data.

We can compare the value of R_{NL} between the CAF state and the LP state, where the spin-valley current and valley current are the origins of R_{NL} , respectively (Fig. 5.14). Comparable values of R_{NL} in CAF (spin-valley Hall effect) and LP state (valley Hall effect) indicates the same order of generation efficiency and decay of the charge neutral current. Theoretically, both valley Hall conductivity and spin-valley Hall conductivity are $4e^2/h$. About the scattering, valley current is thought to be scattered only by atomically sharp defects or at sample edges and the scattering length is of the same order with the width of Hall bar [16, 17]. Scattering of spin-valley current should be limited by inter-valley scattering (width of the Hall bar $1\mu\text{m}$) and spin-flip scattering (a few~ a few tens of μm). Therefore the same order of scattering length is expected for the spin-valley current and valley current. This accounts for the same order of R_{NL} in the CAF state and the LP state.

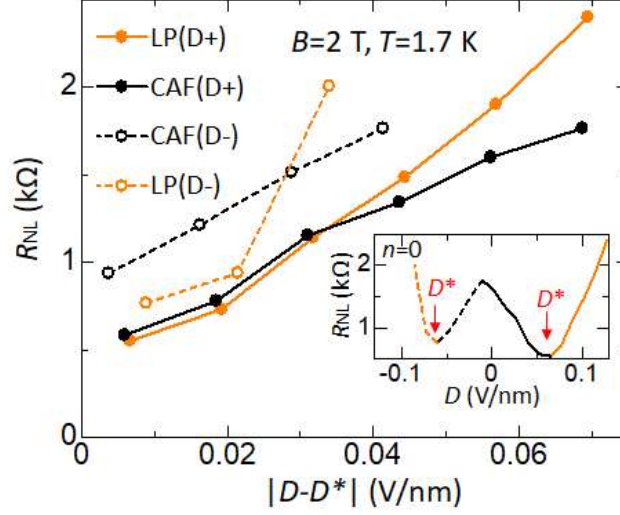


Figure 5.14: Displacement field dependence of R_{NL} for Hall bar 2 R_{NL} at $n = 0$ under the magnetic field $B = 2$ T and temperature $T = 1.7$ K plotted as a function of difference of the displacement field D from the boundary displacement field D^* between the CAF and the LP state. D^* are defined as the minimum of R_{NL} in the D dependence along the $n = 0$ line (denoted by red arrows in the inset). Black (orange) solid line and broken line indicate R_{NL} in the CAF (LP) state for positive and negative D , respectively. Inset: D dependence of the nonlocal resistance at $n = 0$ under the magnetic field $B = 2$ T and temperature $T = 1.7$ K. Black (orange) solid and broken lines indicate the CAF (LP) state for positive and negative D , respectively.

5.7 Elimination of other possible origins of nonlocal resistance

To further make sure the scenario of spin-valley Hall effect, we here discuss four other possible origins of the nonlocal resistance. All four contributions are revealed to be minor.

5.7.1 Current leakage through voltage measurement terminals

Our measurement was performed in the insulating CAF state, where the resistivity reaches 300 kΩ. When the resistivity of the sample is high, electrical current leaks into the voltage amplifiers through the input impedance that are connected to the two measurement terminals (Fig. 5.15(a)). If the resistivity near the two voltage measurement terminals are different due to sample inhomogeneity, the leak current cause the voltage difference between two terminals and detected as nonlocal resistance. The nonlocal resistance caused by this effect is calculated as

$$R_{\text{NL,amp}} = \frac{rR}{R + R_{\text{amp}}/2} \leq \frac{2rR}{R_{\text{amp}}} \leq \frac{2R_{\text{L}}^2}{R_{\text{amp}}}, \quad (5.12)$$

where, R is the two-terminal resistance between current injection terminals, r is the difference of the resistance near the two voltage measurement terminals, and R_{amp} is the input impedance of the voltage amplifier, and we used $r \leq R$ and $R \simeq R_L$ in the second transformation.

In Fig. 5.15(b), we compare the measured R_{NL} with $\frac{2R_L^2}{R_{\text{amp}}}$, which is the upper limit of $R_{\text{NL,amp}}$. $\frac{2R_L^2}{R_{\text{amp}}}$ is 50 ~ 100 times smaller than measured R_{NL} , therefore the current leakage effect is negligible in our nonlocal resistance measurement.

In addition, we measured the nonlocal resistance using two voltage amplifiers with different input impedance, 100 M Ω and 10 G Ω . Figs. 5.15(c) and (d) shows that the measured R_{NL} are identical for the two voltage amplifiers, further making sure that the current leakage is negligible in our measurement.

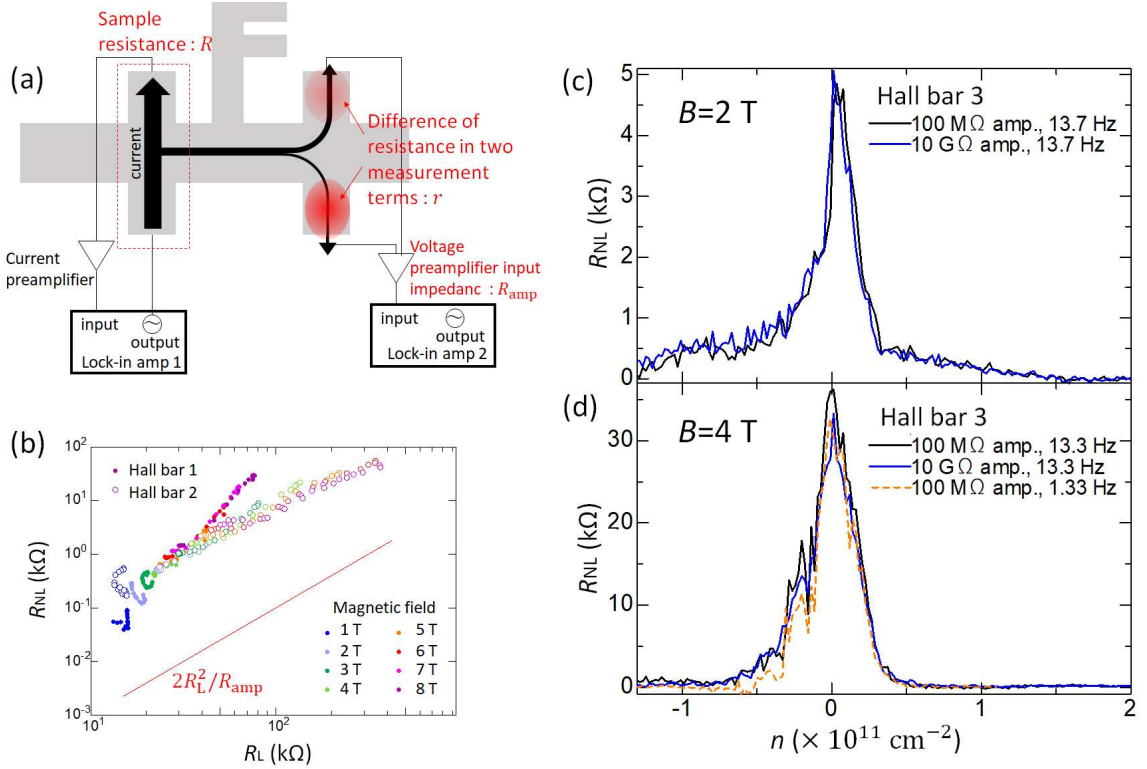


Figure 5.15: Estimation of current flow into the measurement terminals. (a) Schematic description of the current flow into the voltage preamplifier. (b) Measured R_{NL} (circle and open circle) and upper limit of the nonlocal resistance due to current leakage (red line) calculated from Eq. 5.12. (c, d) Carrier density n dependence of R_{NL} at $D = 0$ measured by two voltage amplifiers with different input impedance 100 M Ω (black) and 10 G Ω (blue). Black and blue data are taken at a lock-in frequency of 13.7 Hz and orange data in (d) is taken at a lock-in frequency of 1.33 Hz. The data is taken in Hall bar 3 at $T = 1.7$ K.

5.7.2 Ohmic current diffusion

As we discussed in Eqs. 5.6 and 5.7, Ohmic current diffusion estimated in homogeneous Hall bar is much smaller than observed R_{NL} . However, if the sample have inhomogeneity whose size is comparable with the sample, current diffusion is enhanced. Major cause of such inhomogeneity is bubbles between h-BN and bilayer graphene (Fig. 5.16(a)), whose typical size is several hundreds of nm. To eliminate this possibility, we take a topographic image of the h-BN/ bilayer graphene/ h-BN stack by AFM, and choose a bubble-free region to make the Hall bar sample (Fig. 5.16(b) and (c)). The surface roughness of the Hall bar region is less than 1 nm (Fig. 5.16(c)).

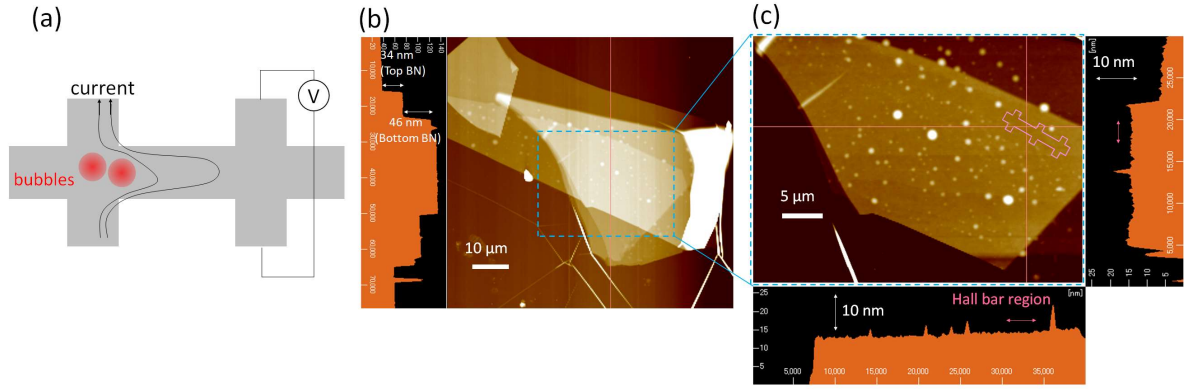


Figure 5.16: Schematic picture of nonlocal resistance due to large obstacles and AFM image of the graphite/h-BN/ BLG/ h-BN stack. (a) schematic picture of the nonlocal resistance induced by large obstacles such as bubbles. (b) AFM image of graphite/ h-BN/ BLG/ h-BN stack used for Hall bar 1. Cross section along the orange vertical line is shown in the left panel. 34 nm and 46 nm step indicate the edge of top BN and bottom BN. Magnified view of the region enclosed by the light blue broken rectangle is shown in (c). (c) Magnified AFM image of the stack. Pink Hall bar shape indicates the position of Hall bar device.

5.7.3 Capacitance effect

Since we perform AC measurement using lock-in amplifiers, capacitance between measurement lines and ground can cause unexpected voltage between terminals. To eliminate this possibility, we measure R_{NL} at different lock-in frequency, 13.3 Hz and 1.33 Hz (Fig.5.15(d)). Identical R_{NL} between two different frequencies indicates that the AC artifact is negligible in our measurement.

5.7.4 Thermal effect

Under a magnetic field, thermal flow is generated perpendicularly to the current due to Ettingshausen effect (inverse Nernst effect). Generated thermal flow causes nonlocal voltage between the voltage measurement terminals due to Nernst effect (Fig. 5.17(a)). Here we

estimate the nonlocal resistance due to this thermal effect based on previous researches of thermal properties of bilayer graphene, and show that this contribution is minor.

The Ettingshausen effect is described by

$$\begin{pmatrix} J_y \\ J_{Qx} \end{pmatrix} = \begin{pmatrix} \sigma_{xx} & \sigma_{xx}S_{yx} \\ -T\sigma_{xx}S_{yx} & K_e \end{pmatrix} \begin{pmatrix} E_y \\ \nabla_x T \end{pmatrix}, \quad (5.13)$$

where, E_y is the electric field along y-axis, $\nabla_x T$ is the temperature gradient along x axis, S_{yx} is the Nernst coefficient, and K_e is the electron thermal conductivity.

Here we make an assumption that the temperature of bilayer graphene is homogeneous because they have six electrodes which act as a heat bath. Based on this assumption, by substituting $\nabla_x T = 0$ in Eq. 5.13, we obtain the heat flow

$$J_{Qx} = -T\sigma_{xx}S_{yx}E_y = S_{yx}TJ_y. \quad (5.14)$$

Then generated heat flow J_{Qx} causes nonlocal voltage $E_{\text{NL,thermal}}$ between the two voltage measurement terminals due to Nernst effect. Nernst effect is described by the inverse matrix representation of Eq. 5.13. By substituting $J_y = 0$ in the inverse matrix representation of Eq. 5.13, we obtain

$$\begin{aligned} E_{\text{NL,thermal}} &= \frac{-\sigma_{xx}S_{yx}J_{Qx,\text{out}}}{\sigma_{xx}K_e + T(\sigma_{xx}S_{yx})^2} \\ &\propto \frac{-\sigma_{xx}S_{yx}J_{Qx}}{\sigma_{xx}K_e + T(\sigma_{xx}S_{yx})^2} \\ &= \frac{-\sigma_{xx}S_{yx}^2TJ_y}{\sigma_{xx}K_e + T(\sigma_{xx}S_{yx})^2}, \end{aligned} \quad (5.15)$$

and therefore,

$$R_{\text{NL,thermal}} \propto \frac{-\sigma_{xx}S_{yx}^2T}{\sigma_{xx}K_e + T(\sigma_{xx}S_{yx})^2}. \quad (5.16)$$

Here, the proportional constant depends on the decay of heat flow.

Based on previous researches on the Nernst coefficient S_{yx} and electron thermal conductivity K_e , we calculated $R_{\text{NL,thermal}}$. Nernst coefficient in monolayer and bilayer graphene is known to be proportional to the temperature and mobility, which is consistent with the Mott's theory [45–47]. Reported value in bilayer graphene is $S_{yx}/T = 1 \mu\text{V}/\text{K}^2$ in samples with mobilities of $1000 \sim 7000 \text{ cm}^2/\text{Vs}$ [47], therefore we assume $S_{yx}/T = 10 \sim 100 \mu\text{V}/\text{K}^2$ in our sample with the mobilities of $70000 \text{ cm}^2/\text{Vs}$.

For the electron thermal conductivity, there is no experimental report for bilayer graphene under a magnetic field. Therefore we adopt the data of numerical calculation [48] (Fig. 5.17(b)).

To determine the proportional constant of Eq. 5.16, we measured the nonlocal resistance at room temperature, where the CAF state should be broken and only possible cause of nonlocal resistance is the thermal effect. We observed $R_{\text{NL}} \simeq 35 \text{ k}\Omega$ at $T=300 \text{ K}$ and $B=2 \text{ T}$ (Fig.

5.17(d)), which is comparable with previously reported value in monolayer graphene and four-layer graphene at room temperature [49, 50].

Using these values, $R_{\text{NL,thermal}}$ is estimated as shown in Figs. 5.17(e) and (f). $R_{\text{NL,thermal}}$ is more than 50 times smaller than observed R_{NL} above $B=4$ T, and has opposite temperature dependence at low temperature below $5\sim 10$ K. Therefore thermal effect is not the main origin of the observed R_{NL} above $B=4$ T. However, below $B=2$ T, $R_{\text{NL,thermal}}$ reaches half of the observed R_{NL} above 10 K. In this magnetic field and temperature regime, we observe deviation from cubic scaling dependence as shown in Fig. 5.11.

From these estimations, we can conclude that the major origin of R_{NL} which has cubic and linear dependence on R_L is not the thermal effect.

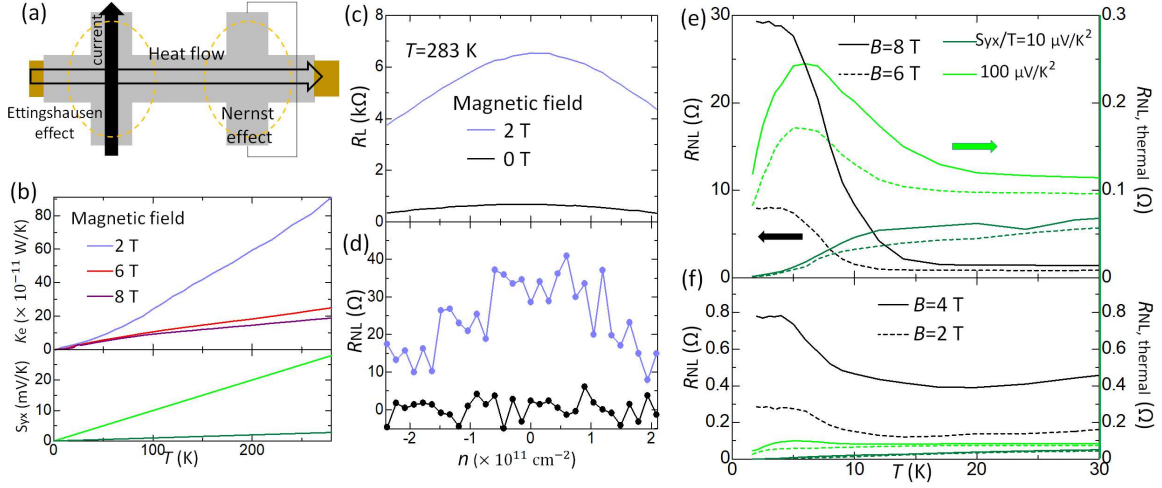


Figure 5.17: Nonlocal transport due to the thermal effect. (a) Schematic picture of the Ettingshausen and Nernst effect as an origin of the nonlocal transport. (b) Electron thermal conductance K_e and Nernst coefficient S_{yx} used for the estimation of $R_{\text{NL,thermal}}$ in (e) and (f). Dark-green and light-green lines correspond to $S_{yx}/T=10$ ($\mu\text{V/K})/\text{K}$ and 100 ($\mu\text{V/K})/\text{K}$, respectively. (c, d) Carrier density dependence of R_L (c) and R_{NL} (d) at $D = 0$ measured for Hall bar 1 at 283 K. (e, f) Measured nonlocal resistance R_{NL} (black lines, left vertical axis) and estimated nonlocal resistance due to the thermal effect $R_{\text{NL,thermal}}$ (green lines, right vertical axis) for $B = 8$ T (solid line, e), $B = 6$ T (broken line, e), $B = 4$ T (solid line, f), $B = 2$ T (broken line, f). Dark-green and light-green lines are the calculation assuming Nernst coefficient of $S_{yx}/T=10$ ($\mu\text{V/K})/\text{K}$ and 100 ($\mu\text{V/K})/\text{K}$, respectively.

5.7.5 Edge transport

If sample edge is more conductive than the bulk, current flows along the edge and causes large nonlocal resistance (Fig. 5.18(a)). Although the CAF state does not have a ballistic edge state, reduction of gate electric field at the sample edge can cause carrier doping and produce low-resistive regions along the edge. To examine this possibility, we fabricated extra

protruding part from between terminals 2 and 3 of the Hall bar (Fig. 5.6). This structure results in 10 times longer edge in Hall bar 1 than Hall bar 2, while dimension of the bulk active area is the same.

If edge transport is much more dominant than bulk transport, Hall bar 1 should have 10 times smaller nonlocal resistance than Hall bar 2. However, as shown in Fig. 5.11, comparable values of R_{NL} are observed in the two samples. This result cannot be assigned to the edge transport but is consistent with the charge neutral current flowing in the bulk as a main contribution of the R_{NL} .

We measured R_{NL} in two more samples having 1 and 50 times longer edge than Hall bar 2. Fig. 5.18(b) shows the peak values of R_L and R_{NL} along the $D = 0$ line obtained at $T = 1.7 \sim 32$ K. They have comparable values of R_{NL} in spite of different edge length, consistent with the scenario of bulk charge neutral current. However, peak of R_L and R_{NL} along the $D = 0$ line in Hall bar 3 and 4 are asymmetric and shifted from each other in the axis of carrier density probably due to inhomogeneous environmental doping, and therefore unsuitable for further analysis other than order confirmation.

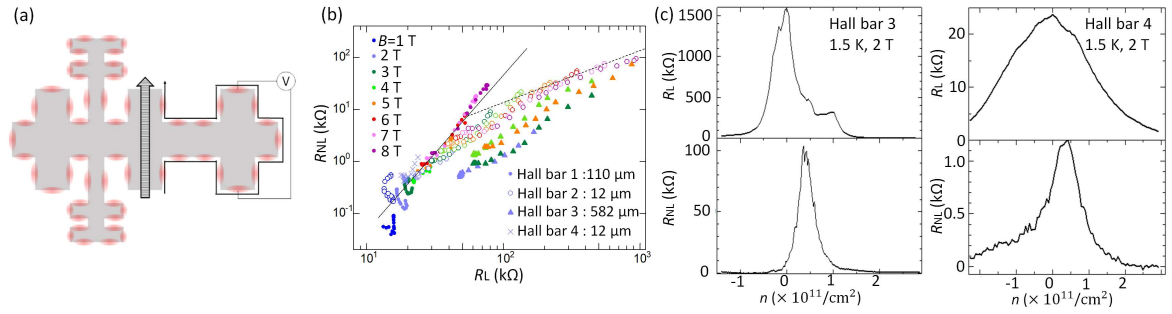


Figure 5.18: Nonlocal transport due to low-resistive edge regions. (a) Schematic description of edge transport as an origin of nonlocal resistance. (b) Peak values of R_{NL} along the $D = 0$ line plotted as a function of peak values of R_L obtained for the temperature of 1.7 to 32 K and magnetic field of 1 to 8 T. Data of the same color were taken under the same magnetic field. Dots, open circles, triangles, and crosses denote the data from different Hall bars. Edge lengths of the Hall bars 1 - 4 are 110 μm , 12 μm , 582 μm , and 12 μm , respectively. The data of Hall bar 1 and 2 are shown in Fig. 5.11. (c) Carrier density n dependence of R_L and R_{NL} at $D = 0$ at 1.5 K for the magnetic field of 2 T measured for Hall bars 3 and 4.

5.8 Conclusion and perspectives

We propose spin-valley Hall effect as a new kind of charge neutral current generation which originates from a new mechanism based on electron correlation and spontaneous symmetry breaking. We employed the CAF state in the quantum Hall regime of bilayer graphene to demonstrate this effect.

Significant enhancement of the nonlocal resistance was observed at the CAF state, and cubic and linear scaling relationship are confirmed as an evidence of charge neutral current genera-

tion and detection via an intrinsic Hall effect. All other possible causes of nonlocal resistance were eliminated from the major origin of the observed nonlocal resistance.

In the nonlocal resistance measurement, we have not directly identified the coupling between spin and valley in the CAF state. To confirm and make use of it, demonstration of conversion between spin current and valley current is possible using a following device (Fig. 5.19).

We also note that application of a perpendicular magnetic field is not necessary in an ultra-clean sample. In suspended bilayer graphene and ABC-stacked trilayer graphene, an insulating state at $D = n = 0$ is observed even under zero magnetic field, which continuously evolves into the $\nu = 0$ state in quantum Hall regime [51–56]. In trilayer graphene, the energy gap exceeds room temperature [52]. Our finding of the new principle to generate charge neutral current can be applied not only to the quantum Hall state but also to any electron correlated systems with spontaneous symmetry breaking.

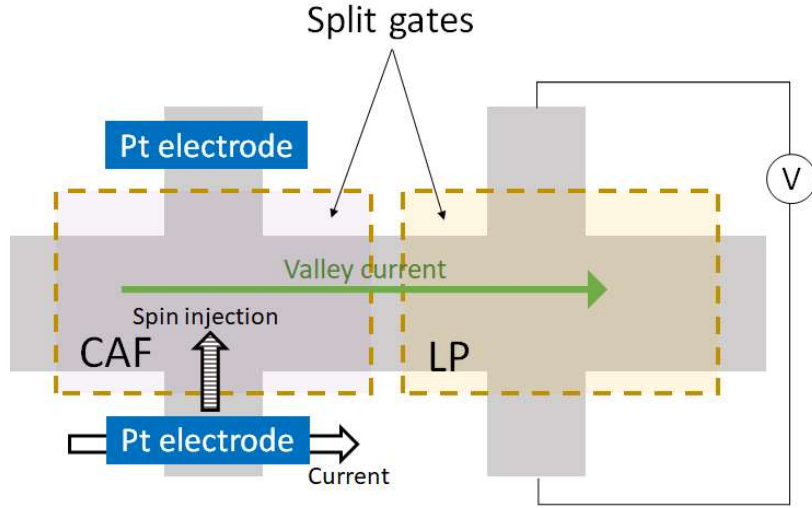


Figure 5.19: Schematic of the device for demonstrate mutual conversion between spin current and valley current. Splitted gates control the displacement field and tune two regions of Hall bar to be the CAF state and the LP state. Platinum electrodes are made in the CAF region to inject spin current via the spin Hall effect of platinum. Injected spin current generate valley current perpendicularly to that. The valley current flow into the LP region and detected as a voltage due to the valley Hall effect. Inverse process can be done by injecting current in the LP region and detecting spin voltage in the CAF region.

Chapter 6

Phase transition in quantum Hall antiferromagnet of bilayer graphene

6.1 Motivation

As discussed in Chapter 4, the $\nu = 0$ state of bilayer graphene can take three different insulating states, ferromagnetic (F), layer polarized (LP) and canted antiferromagnetic (CAF) states [25–27]. Recently new unknown state is observed between the LP and the CAF state. Although fertile quantum phase transitions and temperature-induced phase transitions are expected, most of them are theoretically and experimentally elusive.

For example, the CAF state is expected to exhibit Kosterlitz Thouless transition, but it has not been observed. Quantum phase transition between the CAF and the LP state is expected to be first order phase transition with hysteresis, however, it has not yet been explored experimentally.

In this chapter, we experimentally investigate the quantum phase transition and temperature-induced phase transition using precise conductivity measurement, and to reveal the full phase diagram of the $\nu = 0$ state.

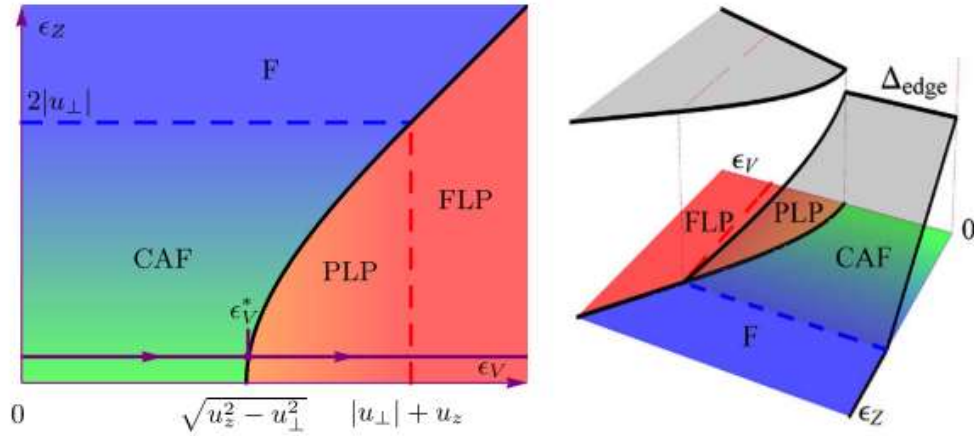


Figure 6.1: Redisplaying of Fig. 4.4.

Phase diagram of $\nu=0$ state of bilayer graphene obtained from theoretical calculation [25]. Left figure is bulk phase diagram as a function of Zeeman energy ϵ_Z and layer polarization energy ϵ_V . Right figure shows the energy gap of the edge state. Only the F state has zero gap edge mode.

6.2	Sample structure	5年以内に出版予定
6.3	Experimental result	5年以内に出版予定
6.4	Discussions	5年以内に出版予定

Chapter 7

Weak localization in ABA-stacked trilayer graphene

7.1 Motivation

Quantum interference in graphene systems is known to be very different from that in ordinal two-dimensional electron gas due to its Berry phase around the Dirac points. Monolayer graphene exhibits weak antilocalization (WAL) in certain temperature range due to its Berry phase of π [57], while bilayer graphene exhibits weak localization (WL) due to its Berry phase of 2π [58].

In trilayer graphene, localization effect depends on its stacking sequence. ABC-stacked trilayer graphene is zero gap semiconductor with Berry phase of 3π around the Dirac points, therefore it is expected to exhibit WAL similar to monolayer graphene. On the other hand, band structure of ABA-stacked trilayer graphene have monolayer-like linear dispersion band and bilayer-like parabolic band (Chapter 2). These bands have Berry curvature of π and 2π , respectively.

Coexistence of monolayer-like band and bilayer-like band result in unique quantum Hall effect [59, 60] and quantum Hall magnetism [61]. However, its influence on quantum interference has not been investigated.

Here we measure magnetoconductance (MC) in ABA-stacked trilayer graphene and explore weak localization effect.

7.2 Sample fabrication

5年以内に出版予定

7.3 Experimental result

5年以内に出版予定

7.4 Discussions

5年以内に出版予定

Chapter 8

Summary and Outlook

We investigated electron correlation effects under existence of internal degrees of freedom in electronic transport of graphene. First, we proposed and demonstrated charge neutral current generation in the quantum Hall antiferromagnetic state of bilayer graphene (Chapter 5). Previously, conversion between the current (or voltage) and charge neutral current via flavor Hall effect is thought to be only possible in systems with spin-orbit interaction or broken spatial inversion symmetry. We challenged this general concept, and propose charge neutral current generation via spin-valley Hall effect, which is possible in centro-symmetric bilayer graphene that has little spin-orbit interaction. Here Hamiltonian is centro-symmetric, but the electron correlation breaks the symmetry spontaneously.

We performed nonlocal resistance measurement to demonstrate charge neutral current generation. Significant enhancement of nonlocal resistance was observed at the canted antiferromagnetic state in $\nu = 0$ quantum Hall state of bilayer graphene. The nonlocal resistance shows linear and cubic scaling dependence on local resistance, which evidences that its origin is charge neutral current generated by intrinsic Hall conductivity. To further confirm it, we considered other possible origins of nonlocal resistances and revealed that the all other origins have minor contribution.

Since the Hall conductivity is spin and valley dependent in the spin-valley Hall effect, mutual conversion between the spin current and valley current will be possible in the future. This opens up a new way of electrical generation and detection of a spin current in graphene with high efficiency.

Second, we explored phase transition in $\nu = 0$ state of bilayer graphene (Chapter 6).

5年以内に出版予定

Third, we investigated weak localization of ABA-stacked trilayer graphene (Chapter 7).

5年以内に出版予定

Acknowledgement

I would like to take this opportunity to thank all of the people who supported me throughout the course of my Ph.D studies.

The present work was performed under the supervision of Prof. Seigo Tarucha and Prof. Michihisa Yamamoto in RIKEN CEMS. First, I deeply thank them for giving me an great opportunity and experimental environment. Their advices provided me with useful information and helped me significantly in planning and performing of experiments. I also thank Prof. Yasunobu Nakamura for fruitful discussion and help for my study during PhD course.

I am really grateful to Dr. Yuya Shimazaki and Dr. Ivan Borzenets. They are experts of this field, and taught me everything including fabrication technique, measurement, and knowledge of physics of two-dimensional materials. Discussions with them were truly helpful.

I greatly thank Dr. Kenji Watanabe and Dr. Takashi Taniguchi in NIMS for providing high quality flakes of hexagonal boron nitride.

I thank all the lab member for supporting me and encouragement. I also thank people in RIKEN liquid helium center and nanoscience support team for their kind support for my experiment.

refereces

- [1] Masato Aoki and Hiroshi Amawashi. Dependence of band structures on stacking and field in layered graphene. *Solid State Communications*, 142(3):123–127, apr 2007.
- [2] K Zou, Fan Zhang, C Clapp, A H Macdonald, and J Zhu. Transport Studies of Dual-Gated ABC and ABA Trilayer Graphene: Band Gap Opening and Band Structure Tuning in Very Large Perpendicular Electric Fields. *Nano Letters*, 13:369, 2013.
- [3] Nikolaos Tombros, Csaba Jozsa, Mihaita Popinciuc, Harry T. Jonkman, and Bart J. Van Wees. Electronic spin transport and spin precession in single graphene layers at room temperature. *Nature*, 448(7153):571–574, aug 2007.
- [4] Wei Han, K. Pi, K. M. McCreary, Yan Li, Jared J I Wong, A. G. Swartz, and R. K. Kawakami. Tunneling spin injection into single layer graphene. *Physical Review Letters*, 105(16):3–6, 2010.
- [5] Marc Drögeler, Christopher Franzen, Frank Volmer, Tobias Pohlmann, Luca Banszerus, Maik Wolter, Kenji Watanabe, Takashi Taniguchi, Christoph Stampfer, and Bernd Beschoten. Spin Lifetimes Exceeding 12 ns in Graphene Nonlocal Spin Valve Devices. *Nano Letters*, 16(6):3533–3539, 2016.
- [6] Wei Han, Roland K. Kawakami, Martin Gmitra, and Jaroslav Fabian. Graphene spintronics. *Nature Nanotechnology*, 9(10):794–807, 2014.
- [7] M. Wojtaszek, I. J. Vera-Marun, E. Whiteway, M. Hilke, and B. J. Van Wees. Absence of hyperfine effects in ^{13}C -graphene spin-valve devices. *Physical Review B - Condensed Matter and Materials Physics*, 89(3):1–7, 2014.
- [8] M B Lundeberg, R Yang, J Renard, and J A Folk. Defect-Mediated Spin Relaxation and Dephasing in Graphene. *Physical Review Letters*, 110(5):156601, 2013.
- [9] Jinsong Xu, Tiancong Zhu, Yunqiu Kelly Luo, Yuan-Ming Lu, and Roland K Kawakami. Strong and Tunable Spin-Lifetime Anisotropy in Dual-Gated Bilayer Graphene. *Physical Review Letters*, 121(12):127703, 2018.
- [10] C. L. Kane and E. J. Mele. Quantum Spin hall effect in graphene. *Physical Review Letters*, 95(22):1–4, 2005.
- [11] Jayakumar Balakrishnan, Gavin Kok Wai Koon, Manu Jaiswal, A. H. Castro Neto, and Barbaros Özyilmaz. Colossal enhancement of spin-orbit coupling in weakly hydrogenated graphene. *Nature Physics*, 9(5):284–287, 2013.
- [12] Jayakumar Balakrishnan, Gavin Kok Wai Koon, Ahmet Avsar, Yuda Ho, Jong Hak Lee, Manu Jaiswal, Seung Jae Baeck, Jong Hyun Ahn, Aires Ferreira, Miguel A. Cazalilla, Antonio H. Castro Neto, and Barbaros Özyilmaz. Giant spin Hall effect in graphene grown by chemical vapour deposition. *Nature Communications*, 5, 2014.

- [13] K. Hatsuda, H. Mine, T. Nakamura, J. Li, R. Wu, S. Katsumoto, and J. Haruyama. Evidence for a quantum spin hall phase in graphene decorated with Bi₂Te₃ nanoparticles. *Science Advances*, 4(11):1–7, 2018.
- [14] C. K. Safeer, Josep Ingla-Aynés, Franz Herling, José H. Garcia, Marc Vila, Nerea Ontoso, M. Reyes Calvo, Stephan Roche, Luis E. Hueso, and Fèlix Casanova. Room-Temperature Spin Hall Effect in Graphene/MoS₂ van der Waals Heterostructures. *Nano Letters*, 19:1074–1082, 2019.
- [15] A. K. Gorbachev, R. V. and Song, J. C. W. and Yu, G. L. and Kretinin, A. V. and Withers, F. and Cao, Y. and Mishchenko, A. and Grigorieva, I. V. and Novoselov, K. S. and Levitov, L. S. and Geim. Detecting topological currents in graphene superlattices. *Science*, 064226(2009):1750–1753, 2013.
- [16] Mengqiao Sui, Guorui Chen, Liguang Ma, Wen Yu Shan, Dai Tian, Kenji Watanabe, Takashi Taniguchi, Xiaofeng Jin, Wang Yao, Di Xiao, and Yuanbo Zhang. Gate-tunable topological valley transport in bilayer graphene. *Nature Physics*, 11(12):1027–1031, 2015.
- [17] Y. Shimazaki, M. Yamamoto, I. V. Borzenets, K. Watanabe, T. Taniguchi, and S. Tarucha. Generation and detection of pure valley current by electrically induced Berry curvature in bilayer graphene. *Nature Physics*, 11(12):1032–1036, 2015.
- [18] Tsuneya Ando. Screening Effect and Impurity Scattering in Monolayer Graphene. *J.Phys. Soc. Jpn.*, 75(7):074716, 2006.
- [19] Kirill I. Bolotin, Fereshte Ghahari, Michael D. Shulman, Horst L. Stormer, and Philip Kim. Observation of the fractional quantum Hall effect in graphene. *Nature*, 462(7270):196–199, nov 2009.
- [20] B. M. Hunt, J. I.A. Li, A. A. Zibrov, L. Wang, T. Taniguchi, K. Watanabe, J. Hone, C. R. Dean, M. Zaletel, R. C. Ashoori, and A. F. Young. Direct measurement of discrete valley and orbital quantum numbers in bilayer graphene. *Nature Communications*, 8(1):1–7, 2017.
- [21] F W Van Keuls, X L Hu, H W Jiang, and A J Dahm. Screening of the Coulomb interaction in two-dimensional variable-range hopping. *PHYSICAL REVIEW B*, 56(3):1161, 1997.
- [22] S E Barrett, G Dabbagh, L N Pfeiffer, K W West, and R Tycko. Optically Pumped NMR Evidence for Finite-Size Skyrmions in GaAs Quantum Wells near Landau Level Filling $\nu = 1$. Technical report, 1995.
- [23] K Moon, H Mori, Kun Yang, S M Girvin, A H Macdonald, L Zheng, D Yoshioka, and Shou-Cheng Zhang. Spontaneous interlayer coherence in double-layer quantum Hall systems: Charged vortices and Kosterlitz-Thouless phase transitions. Technical report, 1994.
- [24] Yafis Barlas, R Côté, K Nomura, and A H Macdonald. Intra-Landau-Level Cyclotron Resonance in Bilayer Graphene. *Physical Review Letters*, 101(9):097601, 2008.

- [25] Maxim Kharitonov. Canted antiferromagnetic phase of the $\nu=0$ quantum Hall state in bilayer graphene. *Physical Review Letters*, 109(4):1–5, 2012.
- [26] MaKhxim Arironov. Phase diagram for the $\nu = 0$ quantum Hall state in monolayer graphene Maxim. *Physical Review B*, 85(15):155439, 2012.
- [27] Maxim Kharitonov. Antiferromagnetic state in bilayer graphene. *Physical Review B - Condensed Matter and Materials Physics*, 86(19):1–5, 2012.
- [28] Joseph G. Checkelsky, Lu Li, and N. P. Ong. Zero-energy state in graphene in a high magnetic field. *Physical Review Letters*, 100(20):2–5, 2008.
- [29] Y. Zhao, P. Cadden-Zimansky, Z. Jiang, and P. Kim. Symmetry breaking in the zero-energy landau level in bilayer graphene. *Physical Review Letters*, 104(6):1–4, 2010.
- [30] Liyuan Zhang, Yan Zhang, M. Khodas, T. Valla, and I. A. Zaliznyak. Metal to insulator transition on the $N=0$ landau level in graphene. *Physical Review Letters*, 105(4):1–4, 2010.
- [31] Z. Jiang, Y. Zhang, H. L. Stormer, and P. Kim. Quantum hall states near the charge-neutral dirac point in graphene. *Physical Review Letters*, 99(10):1–4, 2007.
- [32] A. J M Giesbers, L. A. Ponomarenko, K. S. Novoselov, A. K. Geim, M. I. Katsnelson, J. C. Maan, and U. Zeitler. Gap opening in the zeroth Landau level of graphene. *Physical Review B - Condensed Matter and Materials Physics*, 80(20):1–4, 2009.
- [33] P. Maher, C. R. Dean, A. F. Young, T. Taniguchi, K. Watanabe, K. L. Shepard, J. Hone, and P. Kim. Evidence for a spin phase transition at charge neutrality in bilayer graphene. *Nature Physics*, 9(3):154–158, 2013.
- [34] Kayoung Lee, Babak Fallahazad, Jiamin Xue, David C. Dillen, Kyoungwan Kim, Takashi Taniguchi, Kenji Watanabe, and Emanuel Tutuc. Chemical potential and quantum Hall ferromagnetism in bilayer graphene. *Science*, 345(6192):58–61, 2014.
- [35] Jing Li, Hailong Fu, Zhenxi Yin, Kenji Watanabe, Takashi Taniguchi, and Jun Zhu. Metallic Phase and Temperature Dependence of the $\nu=0$ Quantum Hall State in Bilayer Graphene. *Physical Review Letters*, 122(9):97701, 2019.
- [36] Petr Stepanov, Shi Che, Dmitry Shcherbakov, Jiawei Yang, Ruoyu Chen, Kevin Thilagar, Greyson Voigt, Marc W. Bockrath, Dmitry Smirnov, Kenji Watanabe, Takashi Taniguchi, Roger K. Lake, Yafis Barlas, Allan H. MacDonald, and Chun Ning Lau. Long-distance spin transport through a graphene quantum Hall antiferromagnet. *Nature Physics*, 14(September):1–5, 2018.
- [37] Di. S. Wei, Toeno van der Sar, Seung Hwan Lee, Kenji Watanabe, Takashi Taniguchi, Bertrand I. Halperin, and Amir Yacoby. Electrical generation and detection of spin waves in a quantum Hall ferromagnet. pages 1–16, 2018.

- [38] So Takei, Amir Yacoby, Bertrand I. Halperin, and Yaroslav Tserkovnyak. Spin Superfluidity in the $\nu=0$ Quantum Hall State of Graphene. *Physical Review Letters*, 116(21):1–5, 2016.
- [39] Hans Skarsvåg, Cecilia Holmqvist, and Arne Brataas. Spin Superfluidity and Long-Range Transport in Thin-Film Ferromagnets. *Physical Review Letters*, 115(23):1–5, 2015.
- [40] Yury M. Bunkov and Vladimir L. Safonov. Magnon condensation and spin superfluidity. *Journal of Magnetism and Magnetic Materials*, 452:30–34, 2018.
- [41] E. B. Sonin. Spin currents and spin superfluidity. *Advances in Physics*, 59(3):181–255, 2010.
- [42] So Takei, Bertrand I. Halperin, Amir Yacoby, and Yaroslav Tserkovnyak. Superfluid spin transport through antiferromagnetic insulators. *Physical Review B - Condensed Matter and Materials Physics*, 90(9):1–10, 2014.
- [43] Nguyen Huynh Duy Khang, Yugo Ueda, and Pham Nam Hai. A conductive topological insulator with large spin Hall effect for ultralow power spin–orbit torque switching. *Nature Materials*, 17(9):808–813, 2018.
- [44] Jing Li, Yevhen Tupikov, Kenji Watanabe, Takashi Taniguchi, and Jun Zhu. Effective Landau Level Diagram of Bilayer Graphene. *Physical Review Letters*, 120(4):47701, 2018.
- [45] Yuri M Zuev, Willy Chang, and Philip Kim. Thermoelectric and Magnetothermoelectric Transport Measurements of Graphene. *Physical Review Letters*, 102(9):096807, 2009.
- [46] Joseph G Checkelsky and N P Ong. The thermopower and Nernst Effect in graphene in a magnetic field. *Physical Review B*, 80(8):081413, 2009.
- [47] Chang-Ran Wang, Wen-Sen Lu, and Wei-Li Lee. Transverse thermoelectric conductivity of bilayer graphene in the quantum Hall regime. *REVIEW B*, 82(12):121406, 2010.
- [48] R Ma, L Zhu, L Sheng, M Liu, and D N Sheng. Thermoelectric and thermal transport in bilayer graphene systems. *Physical Review B*, 84(7):075420, 2011.
- [49] D A Abanin, S V Morozov, L A Ponomarenko, R V Gorbachev, A S Mayorov, M I Katsnelson, K Watanabe, T Taniguchi, K S Novoselov, L S Levitov, and A K Geim. Giant Nonlocality Near the Dirac Point in Graphene. *Science*, 332:328, 2011.
- [50] Kalon Gopinadhan, Young Jun Shin, Rashid Jalil, Thirumalai Venkatesan, Andre K Geim, Antonio H Castro Neto, and Hyunsoo Yang. ARTICLE Extremely large magnetoresistance in few-layer graphene/boron-nitride heterostructures. *Nature Communications*, 6:8337, 2015.
- [51] J. Velasco, L. Jing, W. Bao, Y. Lee, P. Kratz, V. Aji, M. Bockrath, C. N. Lau, C. Varma, R. Stillwell, D. Smirnov, Fan Zhang, J. Jung, and A. H. MacDonald. Transport spectroscopy of symmetry-broken insulating states in bilayer graphene. *Nature Nanotechnology*, 7(3):156–160, 2012.

- [52] Y. Lee, D. Tran, K. Myhro, J. Velasco, N. Gillgren, C. N. Lau, Y. Barlas, J. M. Poumirol, D. Smirnov, and F. Guinea. Competition between spontaneous symmetry breaking and single-particle gaps in trilayer graphene. *Nature Communications*, 5:1–5, 2014.
- [53] F. Freitag, J. Trbovic, M. Weiss, and C. Schönenberger. Spontaneously gapped ground state in suspended bilayer graphene. *Physical Review Letters*, 108(7):1–5, 2012.
- [54] R. T. Weitz, M. T. Allen, B. E. Feldman, J. Martin, and A. Yacoby. Broken-symmetry states in doubly gated suspended bilayer graphene. *Science*, 330(6005):812–816, 2010.
- [55] A. Veligura, H. J. Van Elferen, N. Tombros, J. C. Maan, U. Zeitler, and B. J. Van Wees. Transport gap in suspended bilayer graphene at zero magnetic field. *Physical Review B - Condensed Matter and Materials Physics*, 85(15):1–7, 2012.
- [56] Wenzhong Bao, Jairo Velasco, Fan Zhang, Lei Jing, Brian Standley, Dmitry Smirnov, Marc Bockrath, Allan H. MacDonald, and Chun Ning Lau. Evidence for a spontaneous gapped state in ultraclean bilayer graphene. *Proceedings of the National Academy of Sciences of the United States of America*, 109(27):10802–10805, jul 2012.
- [57] F. V. Tikhonenko, A. A. Kozikov, A. K. Savchenko, and R. V. Gorbachev. Transition between electron localization and antilocalization in graphene. *Physical Review Letters*, 103(22):1–4, 2009.
- [58] R. V. Gorbachev, F. V. Tikhonenko, A. S. Mayorov, D. W. Horsell, and A. K. Savchenko. Weak localization in bilayer graphene. *Physical Review Letters*, 98(17):3–6, 2007.
- [59] Thiti Taychatanapat, Kenji Watanabe, Takashi Taniguchi, and Pablo Jarillo-Herrero. Quantum Hall effect and Landau-level crossing of Dirac fermions in trilayer graphene. *Nature Physics*, 7(8):621–625, jun 2011.
- [60] E A Henriksen, D Nandi, and J P Eisenstein. Quantum Hall Effect and Semimetallic Behavior of Dual-Gated ABA-Stacked Trilayer Graphene. *Physical Review X*, 2(1):011004, 2012.
- [61] Yongjin Lee, Jairo Velasco, David Tran, Fan Zhang, W. Bao, Lei Jing, Kevin Myhro, Dmitry Smirnov, and Chun Ning Lau. Broken symmetry quantum hall states in dual-gated ABA trilayer graphene. *Nano Letters*, 13(4):1627–1631, apr 2013.